arXiv:1409.0686v2 [astro-ph.SR] 5 Nov 2014

November 6, 2014

Time sequence spectroscopy of AW UMa. The 518 nm Mg I triplet region analyzed with Broadening Functions[1]

Slavek M. Rucinski

Department of Astronomy and Astrophysics, University of Toronto
50 St. George St., Toronto, Ontario, M5S 3H4, Canada

rucinski@astro.utoronto.ca

ABSTRACT

High resolution spectroscopic observations of AW UMa, obtained on three consecutive nights with the median time resolution of 2.1 minutes, have been analyzed using the Broadening Functions method in the spectral window of 22.75 nm around the 518 nm Mg I triplet region. Doppler images of the system reveal the presence of vigorous mass motions within the binary system; their presence puts into question the solid-body rotation assumption of the contact binary model. AW UMa appears to be a very tight, semi-detached binary; the mass transfer takes place from the more massive to the less massive component. The primary, a fast-rotating star with $V \sin i = 181.4 \pm 2.5$ km s^{-1}, is covered by inhomogeneities: very slowly drifting spots and a dense network of ripples more closely participating in its rotation. The spectral lines of the primary show an additional broadening component (called the "pedestal") which originates either in the equatorial regions which rotate faster than the rest of the star by about 50 km s^{-1} or in an external disk-like structure. The secondary component appears to be smaller than predicted by the contact model. The radial velocity field around the secondary is dominated by accretion of matter transferred from (and possibly partly returned to) the primary component. The parameters of the binary are: $A \sin i = 2.73 \pm 0.11\, R_\odot$ and $M_1 \sin^3 i = 1.29 \pm 0.15\, M_\odot$, $M_2 \sin^3 i = 0.128 \pm 0.016\, M_\odot$. The mass ratio $q_{\rm sp} = M_2/M_1 = 0.099 \pm 0.003$, while still the most uncertain among the spectroscopic elements, is substantially different from the previous numerous and mutually consistent photometric investigations which were based on the contact model. It should be studied why photometry and spectroscopy give so very discrepant results and whether AW UMa is an unusual object or that only very high-quality spectroscopy can reveal the true nature of W UMa-type binaries.

Subject headings: stars: individual (AW UMa) - binaries: eclipsing - binaries: close - binaries: spectroscopic - techniques: spectroscopic

1. Introduction

AW UMa (HD 99946) is a well known, very close, short-period ($P = 0.4387$ d) binary system belonging to the class of "W UMa-type" binary stars. It is sometimes called "Paczynski's star" for the discoverer (Paczyński 1964), who recognized its particular importance for understanding W UMa-type binaries. This is due to its shallow, total, long-duration eclipses with equal depth, the property which directly indicates that the two very different stars have the same surface temperature. The first light curve synthesis models (Mochnacki & Doughty 1972; Wilson & Devinney 1973) showed that photometric variability of AW UMa is in perfect agreement with the model for W UMa binaries presented by Lucy (1968a,b). The Lucy model is based on the assumption of a solid-body rotation which permits the definition of equipotentials; one equipotential is common to both stars. In the case of AW UMa, the agreement of observed light curves with model predictions holds particularly well in spite of the large disparity in masses of the components, as estimated from the Lucy model. Several photometric investigations, continuing to the recent study of Wilson (2008), confirmed that the light curve of AW UMa is in full agreement with the one predicted by the Lucy model for the very small mass-ratio, $q_{\rm ph} = M_2/M_1 \simeq 0.07 - 0.08$. The perfect agreement with the model was reassuring but somewhat unexpected because the model is built on the rather restrictive assumption of the strictly solid-body rotation, i.e. absence of velocity field in the rotating system of coordinates. This would also imply a total absence of any *differential* rotation for the primary F2-type star. In addition, because of the disparate masses, we know that the stars forming AW UMa must be very different in terms of their internal structure, with the more massive primary component ($M_1 \simeq 1.3\,M_\odot$) providing all the energy to be radiated by the whole system; the 10 – 12 times less massive secondary component carries the angular momentum of the system and – within the framework of Lucy's model – is probably an isothermal structure. Yet the common envelope seemed to be somehow oblivious to these structural differences. Indeed, Paczyński et al. (2007) suggested, following Stępień (2006), that the binary consists of a Main Sequence star and a helium star, a core of the former primary of AW UMa, currently submerged in the material of the primary component.

While an abundance of photometric light-curve-synthesis solutions confirmed the applicability of Lucy's model to AW UMa, the radial velocity (RV) data were, for long time, discordant and inconclusive (McLean 1981; Rensing et al. 1985; Rucinski 1992; Pribulla et al. 1999). In general they did not contradict the photometric results, but neither did they contribute much new information because of the poor definition of the radial-velocity orbital amplitudes: On one hand, the secondary was difficult to detect, while the minuscule orbital motion of the primary was hard to measure accurately because of its very broad spectral lines. In contrast to photometric observations, spectroscopic analyses require large telescopes to insure good signal-to-noise values at

[1]Based on observations obtained at the Canada-France-Hawaii Telescope (CFHT) which is operated by the National Research Council of Canada, the Institut National des Sciences de l'Univers of the Centre National de la Recherche Scientique of France, and the University of Hawaii.

short exposures times. The study of radial velocities conducted at the David Dunlap Observatory (DDO) using the 1.9m telescope (Pribulla & Rucinski 2008) was a breakthrough: One can see the improvement by comparing Fig. 2 in Wilson (2008) to Fig. 6 in Pribulla & Rucinski (2008). It was found that the orbital velocity amplitudes clearly indicate a small mass ratio, $q_{\rm sp} = 0.10$, which is however substantially different from $q_{\rm ph}$ by several formal errors of the photometric solutions. From the spectroscopic observations, the secondary component did not seem to look like a star, but perhaps an accretion disk. Furthermore, the primary component showed surface features and an unexplained "pedestal" of large rotational velocities surrounding the rotationally broadened profile. It appeared that AW UMa *is not a contact binary in the sense as defined by Lucy's model, but rather a semi-detached binary; thus, the spectroscopic observations strongly contradicted the photometric solutions which entirely depend on the adoption of this model.* The results were so unexpected that they were taken with disbelief or ignored. Suggestions were made (R. E. Wilson – private communication) that the spectral analysis using Broadening Functions (BF) had some problems which would need an explanation before questioning the well established photometric results. This was unfortunate because (1) one cannot hope to obtain any spectral information from incredibly blended spectral lines without some sort of a deconvolution method, (2) the BF approach shares strengths and weakness with other deconvolution methods utilizing simultaneously many spectral lines to extract velocity information, (3) as such, it provides direct image of the binary in the radial velocity space, but the convenient normalization of the resulting BF's provides a way to verify the assumed spectral type and to spectroscopically estimate the metal content (Rucinski et al. 2013a). Besides, the BF method served very well for the whole DDO program of radial velocities for bright close binaries (summaries in Rucinski (2010, 2012)) and most of W UMa binaries did appear to conform to the Lucy model. But none was so thoroughly analyzed as the brightest observed AW UMa so it is not excluded that their agreement with the contact model could also fail when subject to such scrutiny as is the case of that binary.

The DDO observations of AW UMa by Pribulla & Rucinski (2008) did have weaknesses related to the data acquisition: The 109 spectra were obtained on 12 nights in varying weather conditions, having exposure times ranging between 5.5 and 15 minutes and with a moderate spectral resolution of about 20 km s^{-1} ($R \simeq 15,000$). Observations described in the current paper improve on all of the above numbers by observing AW UMa continuously on three consecutive nights using high resolution spectra. The CFHT spectrograph had several times higher throughput and efficiency while the telescope was two times larger than that used at DDO. The available spectra cover practically the whole optical region. The current paper describes the data for the Mg I window for a direct comparison with the DDO results. Further analyses of the same spectra are planned for the future publications.

Section 2 and 3 describe the observational data and their processing using the Broadening Functions technique. Properties of the primary component of AW UMa are discussed in Section 4 and 5 while properties of the secondary component are discussed in Section 6. Section 7 summarizes properties of AW UMa as a binary system. Section 8 contains conclusions and a discussion of

potential future work.

2. CFHT observations

The observations of AW UMa were obtained on the nights of 11 – 13 March 2011 using the Canada-France-Hawaii Telescope (CFHT) and its Espadons spectrograph working in the spectro-polarimetric mode. The nominal spectral resolving power was $R \simeq 68,000$. Four consecutive observations with different positions of the polarization analyzer can be used to determine the Stokes circular polarization parameter V. In total, 146 series of polarization measurements were obtained; their preliminary analysis by Dr. J.-F. Donati (private communication) indicated no circular polarization at a noise level as low as 0.01% and thus no obvious signature of surface magnetic fields. For that reason, we used all $146 \times 4 = 584$ individual observations of AW UMa leaving the polarization issues for a possible future detailed re-analysis. The exposure times were 90 seconds and the median spacing between observations was 125 seconds. Some breaks in the continuous monitoring took place for observations of four standard stars and for the queue-observing housekeeping (visible as gaps in the figures below).

The data were processed by the CFHT pipeline "Libre-Esprit" (Donati et al. 1997)[2]. While the full spectra extended from 370 to 1,050 nm, we use here only the data in the window around the Mg I triplet, 506.05 – 528.80 nm, with three echelle orders contributing to this segment. This choice was made to permit a direct comparison with the results of Pribulla & Rucinski (2008). The orbital phases were calculated following the discussion of the photometric eclipse moments in Rucinski et al. (2013b) which was based on the literature data merged with the recent *MOST* satellite results obtained soon after the CFHT observations. The linear elements for the primary eclipse just before the start of the CFHT observations were $HJD - 2,400,000 = 55631.6498 + 0.43872420 \times E$, where E is the epoch. The nightly ranges of HJD and phase (calculated from the above epoch) are tabulated in Table 1. Altogether, slightly more than 5 orbital cycles of AW UMa were observed.

3. The Broadening Functions technique

The Broadening Function (BF) technique was introduced for the study of AW UMa some time ago (Rucinski 1992) and since then has been considerably improved. It was extensively used during the DDO radial velocity studies of short-period binary stars between 1999 and 2008, which provided radial-velocity orbital data for 162 systems, see Rucinski (2010, 2012). As with the current observations, the previous, 1992 study of AW UMa was also based on the CFHT data, but used a relatively low throughput spectrograph–detector combination and did not not offer any substantial progress in our understanding of the binary.

[2]http://www.cfht.hawaii.edu/Instruments/Spectroscopy/Espadons/Espadons_esprit.html

In essence, the BF technique is the determination of the Doppler broadening kernel B in the convolution equation, $P(x) = \int B(x')T(x - x')dx'$, where P is the spectrum of the binary and T is the spectral template. P and T are of the length of the adopted window. The window used here, 506.05 – 528.80 nm corresponds to the span of $\simeq 13,200$ km s^{-1} in radial velocities. The lengths of the Broadening Function B is selected on one hand to be much shorter than P and T to provide adequate over-determinacy, yet long enough to adequately cover the whole range of B with a baseline on both sides of the broadened profile. In the current study, the adopted BF range was $[-495, +495]$ km s^{-1} permitting solution of the linear equations representing the convolution using the least-squares method with the 13-fold over-determinacy. The BF technique is very similar to the Least Squares Deconvolution (LSD) method introduced by Donati & Collier Cameron (1997) and Donati et al. (1997) in that it is a fully linear approach and thus far superior to the Cross-Correlation Function (CCF). The BF technique normalizes the results in such a way that the integral over all velocities, $I = \int B(v)dv$, is equal to unity for an exact spectral match of the P and T. This property and the dependence of I on the spectral type and metal abundance was used for spectroscopic estimates of the metallicities of W UMa-type binaries in Rucinski et al. (2013a).

During the DDO program, we used the actual spectra of slowly-rotating standard stars of matching spectral types as templates T. This permitted direct calibration of the zero point of the radial velocities and assured inclusion of all lines in the spectral window. Although spectral-standard stars were observed, the CFHT data did not permit this approach because the tiny deficiencies in the pipeline processing (in transformations from the 2D echelle images to 1D spectra, the same for P and T) became strongly amplified after the array-inversion operation. Instead, we used a model spectrum computed for the spectral type of AW UMa by Dr. Jano Budaj. The model spectrum covered the whole optical spectrum for $T_{\rm eff} = 7250$ K, $\log g = 4.5$ (cgs), with an assumed solar metallicity, a micro-turbulence of 2 km s^{-1} and no macro-turbulence.

The CFHT pipeline-processed spectra were sampled at intervals of 1.8 km s^{-1}, but to insure the high quality of the BF's, they were smoothed with a Gaussian with a FWHM of 8.5 km s^{-1}, which is equivalent to the spectral resolving power of $R \simeq 35,000$. At this resolution, the input spectra have the high signal-to-noise of $(S/N)_{\rm sp} \simeq 200 - 500$, depending on the orbital phase of the binary, the instantaneous brightness of the star and on the presence of cirrus or changes in the air mass; the median for all spectra is $(S/N)_{\rm sp} \simeq 345$. The BF determination involves inversion of very large arrays leading to a decrease in the signal-to-noise. For the current choice of the BF length $(S/N)_{\rm BF} \simeq 30 - 115$, with the median $(S/N)_{\rm BF} = 57$. The BF errors are distributed randomly along the function and do not depend on its local value. The BF's for all observed spectra are available for retrieval, as in Table 2.

Broadening Functions for four cardinal orbital phases are shown in Figure 1. The BF technique produces functions which have integrals normalized to unity for the perfect spectral match of the template spectrum to the observed spectrum in terms of the overall strength; any deviations in the spectral type or metallicity manifest themselves through the integral being systematically smaller or larger than unity. For the adopted spectral model template of a F2V star, the integrals have

the median value of 1.1; see the lower curve in Figure 2. The deviations from unity may be interpreted that the spectral type of AW UMa is slightly later than the F2V model template. The corresponding shift in color would be then $\Delta(B-V) \simeq +0.03$ (see Figure 3 in Rucinski et al. (2013a)). The shift should not necessarily be taken as a disagreement between the color of the star and the template used, because the spectral type of AW UMa has never been determined through spectral classification. Instead, it has always been evaluated by matching to the colors of MS stars[3]. The small variation in the observed BF-integral within 1.09 – 1.12, with a slight increase over the half of the orbit centered on the secondary eclipse (phases $0.25 < \phi < 0.75$) may be interpreted as a tendency towards lower temperature for the part of the orbit when the small star is behind the more massive star. This does not agree with the standard contact model which predicts reddening to take place during both eclipses.

The normalization property of the BF's to the integral of the template offers a powerful check on their capability to capture the whole light curve variations; it also permits one to ascertain that the phase variations observed spectroscopically correspond to the same part of the binary which produces the photometric light variations. The check is based on fits of the rotational profile r to the primary star feature, $R = S_1 \times r(V \sin i, u) + S_0$, as described in Section 4.1 below. Here we use the normalization factor S_1 and relate its time variations to the integrated rotation profile, C, which is a constant. The ratio C/S_1 tells us how much light (i.e. which portion of the integral $I = \int B dv$) comes from the whole binary system relative to the total light from the primary component. This leads to a rather well defined "light curve" as in the upper panel of Figure 2. This curve has been obtained entirely from the strength of the spectral lines, without any reference to photometry. The amplitude of the curve is about 16% or 0.19 in magnitudes which is $\simeq 3\%$ less than observed photometrically in the V-band (Pribulla et al. 1999). The curve is not perfect as it shows apparent deterioration in rotational-profile fits during the primary eclipse when the secondary component transits the disk of the primary. The inner contacts of "totality", as delineated by cusps in the curve at the primary eclipse (Figure 2) are located at the phases -0.070 and $+0.053$, each determined to ± 0.003. The less-well defined inner contact phases for the secondary eclipses, when the secondary disappears behind the larger star, are -0.080 and $+0.055$ (± 0.005). All these contacts are similar to the well determined photometric contacts (± 0.062) which play the essential role in the method of Mochnacki & Doughty (1972). We return to the eclipse contact phases when discussing the spectroscopic estimates of the secondary component size in Section 6.2 and in Table 5.

Thanks to the linear properties of the BF's, plots such as in Figure 1 are expected to be faithful representations of the binary in the radial-velocity space. But this is true on condition of a strict correspondence of the photospheric star spectrum to the template spectrum. This condition must be obeyed by any technique that utilizes spectral deconvolution, not only the BF but also the CCF and the LSD methods. Without these methods we could not analyze spectra equally complex as

[3]This discrepancy may also result from the systematic differences between intensity and flux spectra for strongly distorted stars which we disregard here.

those of AW UMa, but there is a cost involved: The presence of emissions at any place on the star or of local variations of temperature may distort the BF's and spoil the radial-velocity mapping of the stellar surfaces. In fact, the spectral lines appearing fully in emission would produce a negative BF. Thus, when the spectral lines are shallower than in the template, then the BF will show depressions, but when the lines are deeper, then the BF will be stronger. The lines can be deeper for surface regions of lower temperature while the lines can be shallower for higher local surface temperatures or when the lines are filled in by emissions. For the spectral type of AW UMa, the Fe II lines dominate strongly over the Mg I 518.4 nm triplet lines in our window (Rucinski et al. 2013a). The magnesium lines are not expected to show emission in this temperature regime, although we cannot entirely exclude this possibility. As we will see, our results reveal a very complex picture of AW UMa which is hard to explain through strictly geometric causes alone. Thus, it is possible that some depressions in the BF's are not due to dark photospheric spots but, rather, reflect the presence of emissions (or – correspondingly – of a shallower atmospheric source function than in the template model); conversely, segments in the BF's of unusually high intensity may indicate lower local temperatures.

4. The primary component

4.1. The rotational profile fits

The spectral features of the primary component were fit for all BF's by rotational profile of a rigidly rotating, limb-darkened star: $R = S_1 \times r(V \sin i, u) + S_0$, where $r(V \sin i, u)$ is the center-normalized profile (as given in many text-books, e.g. Gray (2005)) and S_i are the two fit constants. The profile r involves two stellar parameters, the projected equatorial velocity, $V \sin i$, which is basically the scaling constant of the X-axis, and the limb darkening coefficient, here assumed constant, $u = 0.6$. The profile centroid position, V_1, gives the mean velocity of the primary star and is the fourth free parameter of the fit.

The least-square fits were done using the upper 50% of the profiles (within $-142 < V < +142$ km s^{-1} for the assumed mean $V \sin i = 181.4$ km s^{-1}, see below in Section 4.2), to avoid complications from the "pedestal" at large rotational velocities around the primary (Section 4.4). Also, one can expect a lesser influence of the equatorial flows on the rotational profile for high latitudes of the primary component. The typical fits can be seen in Figure 1.

The rotational profile fits were well determined for all phases, as can be judged by the small scatter in the fit parameters. The baseline level S_0 has a very small scatter around zero with the median error of $\pm 6 \times 10^{-6}$ in the integral BF units (as in Figure 1); when expressed relative to the maximum strength (called below "i.u."), the median error of S_0 is only 0.01%. The scaling factor S_1 shows systematic variation with phase, as shown in Figure 2, also with a very small scatter. In that figure the factor S_1 is plotted – for convenience – as C/S_1, where C is the integral of the rotational profile. The resulting curve is very similar to the photometric light curve of

AW UMa. The similarity of the shape is in fact expected (for an invariable primary) as was discussed in Section 3 thanks to (1) the built-in normalization of the BF integrals to the integral of the template spectrum and (2) the very weak variation of the apparent spectral type with orbital phase. Since the brightness and $V \sin i$ of the primary are apparently constant with phase, instead of the units resulting from the BF normalization (as in Figure 1), we will use the central intensity (S_1) as a more convenient "intensity unit" (i.u.) in the subsequent plots and figures.

The results shown in Figure 2 were obtained strictly spectroscopically, but they represent a very reasonable light curve of AW UMa which confirms the proper system of photometric phases used in this paper. The figure also shows that most of the orbital phases were observed multiple times; the single-night coverage took place only for two narrow phase intervals 0.98 – 0.01 and 0.75 – 0.80.

During the phase interval -0.07 to $+0.07$, the rotational-profile fits are distorted by the projection of the secondary component during its transit in front of of the primary star. This is reflected in the lower values of S_1 and by the upward spike in the very centre of the primary eclipse in Figure 2. The appearance of the secondary component in the data is discussed further in Section 6.

4.2. The rotation velocity

Values of the projected equatorial velocity of the primary component, $V \sin i$, determined from the individual broadening functions are shown versus the orbital phase in Figure 3. The median value which will be used below, 181.4 ± 2.5 km s^{-1}, has been determined for the phase interval $0.25 < \phi < +0.75$ (299 data points). The wide phase range around the primary eclipse, which was excluded, resulted from indications that gas motions around the secondary component may distort velocities of the primary star (see Section 4.3). Some traces of systematic phase trends and nightly variations in $V \sin i$ indicate that gas motions may be present at all phases and may influence the primary BF feature even within the upper 50% of its height.

It has been long recognized that AW UMa is observed with an edge-on orbit, as implied by the long duration of the total eclipses. Thus, for solid-body rotation, the value of $V \sin i$ should be very close to the equatorial velocity of the primary. Assuming that it rotates in synchronism with its orbital motion, $V \sin i = 181.4$ km s^{-1} implies a radius of $1.49\,R_\odot$, which is fully consistent with a F2V star.

It is possible that the actual $V \sin i$ is smaller than the assumed median value, as indicated by a drop in its value to about 177 km s^{-1} at the very center of the secondary eclipse (phase 0.5, the small star behind), see Figure 3. This would mean that the upper part of the BF profile is almost always broadened by gas streams. However, variations in the individual determinations of $V \sin i$ within the secondary eclipse between the individual nights force us to leave this issue as open for now.

4.3. The orbital motion of the primary

The solution of the orbital motion of the primary component of AW UMa was based on the 299 data points in the phase range 0.25 – 0.75. Within this range, the motion of the primary appears to be sinusoidal (see Figure 4). Fits of the rotational profile to the primary component BF peaks may be affected by complications due to the presence of the "pedestal" below the level of about 0.4 of the BF maximum (see the next Section 4.4) and by the surface inhomogeneities when the cut-off level for the fits is set too high. It was determined that radial velocities measured with the low cut-offs within the range of 0.45 to 0.55 of the maximum peak were least affected by both complications. Three sets of rotational profile fits were accordingly obtained for the upper 55%, 50% and 45% of the observational BF's. The results for all phases are tabulated in Table 3.

The sine fits for the phase range 0.25 – 0.75 for the three levels of the cut-off are given in Table 4. They are of high quality with the typical mean error of $\simeq 1.0$ km s^{-1} per point. Such a measurement error, perhaps large by today's standards, is unprecedentedly small for a component of a W UMa binary; when compared to the total width of the primary profile ($2 \times V \sin i$) it amounts to only 0.3%. The individual radial velocity determinations for the three cut-off levels are non-random and correlated (Figure 5); obviously, these intrinsic variations increase the above estimate of the fit error per point. We see a systematic dependence in the derived values of V_0 and K_1 on the cut-off level; this dependence may possibly be modelled once a correct model of the binary is developed. For the final orbital solution, we adopt the mean values of V_0 and K_1, as listed in Table 4, with the uncertainties estimated from the scatter between the three sets of the parameters: $K_1 = 28.37 \pm 0.37$ km s^{-1}, $V_0 = -15.90 \pm 0.12$ km s^{-1}. The orbital amplitude K_1 is small when compared with the width of the primary profile: The star moves by only 7.8% of its full width in radial velocities. The masses of the AW UMa components resulting from the above orbital elements are discussed in Section 7.1.

The RV data deviate from the sine curve over the wide range of orbital phases close to the primary eclipse (at least within $-0.8 < \phi < +0.2$), which implies that the radial velocity curve of the primary component is perturbed by the projection of the secondary component. The perturbations show some similarity to the "Rositter - McLaughlin effect" which – in terms of the RV amplitude – was noted by Wilson (2008), on the basis of much less detailed observations, to be unexpectedly small or perhaps entirely absent. Our observations confirm that the eclipse disturbance is indeed much smaller than predicted by Lucy's contact model. However, it extends in the orbital plane far from the centre of the secondary component. In fact, judging by the extent of the perturbation, the secondary appears to be even larger than the primary component. This may be taken as one of several indications that the secondary is not a star filling its Roche lobe but rather a flattened structure. The radial-velocity disturbances within the primary eclipse ($-0.8 < \phi < +0.2$) are asymmetric relative to the line joining the stars; a distinct isolated feature around the phase +0.05 was observed on all three nights, see Figure 4.

4.4. The pedestal

An additional RV component is observed at radial velocities of about 150 – 250 km s^{-1} relative to the center of the primary component. It is called the "pedestal" because it presents, in Figure 1, as an extended base of the central rotational profile. It is best seen when the same rotational profile (assumed $V \sin i$ = 181.4 km s^{-1} and scaled by S_1, see Section 4.1), is subtracted from individual BF's, as in Figure 6. The pedestal was discovered by Pribulla & Rucinski (2008). No interpretation was offered there except for noticing that it must be produced by an optically thick material (to produce the same absorption spectrum as the star) moving around the primary at high rotational/orbital velocities. While it is observed at both negative and positive velocities relative to the center of the primary, it is better defined for velocities opposite to those of the secondary component. The phase dependence of the integrated intensity of the pedestal, after removal of portions of the orbit which can be affected by the secondary star, is shown in Figure 7. The pedestal intensities, when expressed in units of the integrated rotational profile, vary at the level of 2.5% to 4% with the phase, following the double cosine curve, as expected for an elliptical distortion. The width of the pedestal does not seem to be phase dependent and stays within about 50 km s^{-1} beyond the rotational profile, so that the variations are mostly due to the changing brightness within it.

At this point one cannot say if the pedestal originates *on the primary component* as a belt of rapidly-moving gas or a disk in the orbital plane, but *outside the star*. The moderate intensity of the pedestal suggests that this distinction is almost immaterial and that the gas must be rather strongly confined to the equatorial plane.

5. Surface inhomogeneities on the primary component

5.1. Types of features

The two-dimensional images of the velocity field over the disk of the primary component of AW UMa are presented in Figures 8 – 10. The figures show surface features which are not expected for a simple rotating star. The figures have been obtained by (1) shifting the velocities to the center of the primary component using the value of K_1 (Section 4.3), (2) subtracting the best-fitting rotational profiles from the BF's and (3) re-sampling the individual deviations into a uniform phase grid at the step of 0.0033 in phase (125 sec in time).

In addition to the pedestal discussed in Section 4.4, which presents in the figures as two vertical ridges along the edges of the rotational profile, one sees two main types of feature on the surface. We call them "ripples" and "spots". Both of them appear to follow the rotational motion of the primary, but several details allow to distinguish them in 2D figures, so we discuss them separately.

5.2. Ripples

In the image of deviations from the rotational profiles in Figures 8 – 10, the ripples form a grid of tenuous, inclined lines crossing the whole range of velocities which are related to the primary component. They are narrow with the width approaching the RV resolution of our data. The ripples can be distinguished from the spots by their velocity dependence: The spots tend to curve towards the stellar disk edges (somewhat similarly to the arcsin function) and do not extend beyond $\pm V \sin i$; in contrast, some of the ripples appear to continue into the pedestal, i.e. outside the stellar disk. Thus, the gas responsible for the formation of the pedestal and the ripples may have the same origin. The ripples are surprisingly straight which may indicate that the physical structures causing them are located above the stellar surface.

Four rectangular sections of Figures 8 – 10, covering phases 0.60 – 0.87, 3.12 – 3.30, 5.09 – 5.34 and 5.36 – 5.51 and at the center of the disk, within ± 130 km s^{-1} in velocities were analyzed for the frequency content in the deviations from the rotational profile. They were selected so as to avoid obvious spots or traces of the secondary transiting the primary. For each section, the FFT analysis was performed on all available observational BF's, ranging in number between 42 and 72 per segment. The median amplitudes for each segment are plotted in the upper part of Figure 11 versus the spatial (the RV space) frequency expressed in the language of non-radial pulsations as l-degree modes. The amplitudes appear to rise toward low frequencies (i.e. larger RV scales), but cannot be determined for $l < 30$ because of the finite extent in the radial velocity range and the presence of spots. At the lowest accessible spatial frequencies the amplitudes reach $\simeq 0.008$ i.u. Thus, the ripples are faint, and their detection at levels even below 0.001 i.u. has been only possible thanks to the high quality of the CFHT observations. The frequency content of the ripple amplitudes partly reflects the wispy structure of the thin ripples as the individual strands sometimes show larger contrast with intensities > 0.01 i.u.

The ripples may possibly be both bright and dark, but this obviously depends on the way how the rotational profile is fit and subtracted. If some are bright, as it seems for a few extending into the pedestal, this property would distinguish them from the dark spots. Taking into account the properties of the BF's (Section 3), the bright strands may in fact have a lower temperature than the surroundings as then BF features become stronger in intensity (provided the matter remains optically thick).

The best defined ripples with amplitudes larger than about 0.005 – 0.007 i.u. (depending on limits set by the local confusion) were analyzed in 2D images (Figures 8 – 10), for their duration (expressed in phase ϕ) and the slope $dV/d\phi$ at the center of the primary profile, i.e. at the meridian crossing point. While we do not see any regularities in the durations, the slopes (counted per one rotation synchronized with the orbital period) give some information on typical drift velocities across the stellar disk. The lower panel of Figure 11 gives the histogram of the drift velocities for the 35 measured, stronger ripples. While the accuracy is low, typically ± 25 km s^{-1} and there may exist a genuine spread in the ripple slopes, the median $dV/d\phi/2\pi = 170 \pm 21$ km s^{-1} is consistent with

the projected equatorial velocity, $V \sin i = 181.4$ km s^{-1}. Thus, the ripples appear to participate in the rotation of the primary component. Their straight shape and extensions into the pedestal are then hard to explain as surface features; they may very well be structures above the surface, but sharing the rotation of the star.

5.3. Spots

Spots are inhomogeneity features on the primary component which are dark in the BF's and appear within $\pm V sini$, but do not extend into the pedestal. Thus, they seem to be confined to the range of the surface radial velocities.

The spots are always best visible at the negative-velocity side of the BF's where they can be as deep as 0.1 i.u. As can be seen in Figures 8 – 10, the spots emerge at negative velocities slowly, curving upward as expected for surface features and then accelerating in radial velocities (turning more horizontal) towards the sub-observer meridian. Their apparent drift at the meridian crossing is unexpectedly slow: In the 2D images they are more vertical than the synchronous rotation would imply; if they shared the surface rotation as given by $V \sin i$, then their horizontal drifts would be much faster across the profile. The mean drift velocity at the meridian is relatively uncertain, $dV/d\phi/2\pi = 120 \pm 30$ km s^{-1}, because most spots do not cross the central meridian to reach positive velocities; usually they disappear while still approaching the observer.

If interpreted as rotational velocities, the slow drift velocities at the meridian of $\simeq 120$ km s^{-1} would imply a rotation period about 3/2 longer than the one resulting from $V \sin i$ and the synchronous rotation rate. Such a surprisingly slow rate finds some support in an attempt to phase the reoccurrence of the spots, as shown in Figure 12. In this figure the spot drifts are shown for the periods which appear to give the best clustering of the individual lines, of 1.00, 1.46 and 1.52 times $P_{\rm orb}$. While an exact alignment of the tracks is hard to achieve for any period tested, the scatter visibly diminishes for the slow rotation rates of around $3/2 \times P_{\rm orb}$. Such a slow rotation rate is unlikely, given the excellent fits of the rotational profile to the upper parts of the primary star BF profiles. Thus, we may suspect that the spots are due to surface structures moving *relative* to the stellar surface with their own, slow rotation rate. The Doppler mapping of such features would be very difficult to achieve for the short rotation period of AW UMa and if the differential rotation rate is indeed as large as $\simeq 50\%$.

The lack of an obvious Stokes V signal (Section 1) suggests that spots are non-magnetic structures, but it is difficult to determine what is the nature of the spots and why do they appear dark. They may be genuinely dark, but it is hard to imagine photospheric spots which would lower the spectral continuum locally but have not already been detected in photometry (although a comparison of the light curves by Pribulla et al. (1999) does show significant seasonal changes in AW UMa light curves). More likely the spots are visible only spectroscopically and possibly only through the use of the spectral deconvolution. This would happen if the spectral lines are

locally shallower than expected, as then depressions in the BF's would appear. The lines could become more shallow due to filling-in by emission or to locally higher gas temperatures. This matter remains unresolved at this point.

Irrespectively of the period assumed for the spot movement rate, synchronized with $P_{\rm orb}$ or equal to $3/2P_{\rm orb}$, as in Figure 12, the spots tend to appear mostly at the sub-secondary and the opposite "ends" on the primary component, along the line joining the stars. This may be due to instabilities and/or condensations in flows predicted by Oka et al. (2002) for the mass-loosing component of a semi-detached binary. According to these model computations, the flow should take place from the high-pressure polar regions to the low-pressure equatorial regions with the latter situated along the line joining the mass centers. The high-pressure counter-rotation in the polar regions in the model of Oka et al. (2002) may have links to the puzzling visibility of the spots only at the negative-velocity side: If the spots are extended but thin, they may be curved in such a way as to be visible at similar velocities at the negative side, but distributed in velocities (hence harder to detect) while on the positive side of the profile.

6. The secondary component

6.1. The velocity field around the secondary

AW UMa shows a systematic period change $dP/dt = -5.3 \times 10^{-10}$ or -1.9×10^{-7} day/year (Rucinski et al. 2013b) which is typical for about a quarter of W UMa type binaries for which such changes have been detected (Kubiak et al. 2006); most of them show smaller, randomly distributed period changes. When interpreted as resulting from the conservative mass transfer from the more massive to the less massive component, the mass exchange rate (estimated using Eq. 4.56 in Hildtitch (2001)) is: $dM/dt = (1/3)\,(M_1 M_2)/(M_1 - M_2)\,(dP/dt)/P \simeq -2.1 \times 10^{-8} M_\odot$/yr. Note that this is the *net mass transfer rate*: The actual amount of the mass flowing from the primary to the secondary may be larger, as part of the flow may return to circle around the primary component and feed the pedestal. The mass-transfer process leads to accretion phenomena clearly visible spectroscopically on and around the secondary component. According to Pribulla & Rucinski (2008), the secondary may actually be an accretion disk or a star submerged in a disk-like structure.

Figure 13 shows profiles obtained by averaging nine individual BF's observed within ± 0.015 in phase around each of the three fully observed orbital quadratures. The secondary shows a double-peaked shape which is characteristic for an accretion region. The shape changes from night to night in intensity and in spacing between the peaks. For the three observed quadratures, the peak separation (measurable to about ± 3 km s^{-1}) varied distinctly: 80, 98 and 65 km s^{-1} with the mean half-separation of 40.5 ± 4.8 km s^{-1}. The outer wings, beyond the peaks, outside of the inner $\pm(60 - 70)$ km s^{-1}, were the same for the two quadratures when the secondary was moving away, but they were quite different for the single quadrature when the secondary was approaching us; this was due to the influence of the pedestal which was apparently different when seen from

both sides of the binary. The mean velocities (relative to the primary mass center), determined as averages from the peak positions at the three quadratures, are surprisingly similar: −320.6, +310.8, +311.2 km s^{-1}. This gives the mean $K_1 + K_2 = 314.2 \pm 3.2$ km s^{-1}. This number, taken with $K_1 = 28.37 \pm 0.37$ km s^{-1}, leads to the mass ratio $q_{\rm sp} = M_2/M_1 = 0.0991 \pm 0.0014$. We will use the values of K_1 and q for determination of the component masses in Section 7. Here we note that the error of $K_1 + K_2$ as given above may be fortuitously small as it is based on only three determinations; we will use ± 0.003 as the error of $q_{\rm sp}$.

A major difference in the interpretation results from two possible assumptions on what we actually see as the secondary component, an accretion disk or manifestations of accretion processes on the surface of a star. For a stable accretion disk, the distinct peaks in the RV profile are produced by the slow-moving material at the outer rim of the disk, while the extended wings outside of the peaks are formed by the large-velocity matter in the innermost parts of the disk (Smak 1981, 1993). To be visible in the BF's, such a disk would have to consist of optically thick matter to produce a stellar spectrum with the same absorption lines as for the stellar surface. Obviously, the geometry of an optically thick disk would require an axis inclination of $i \neq 90$ degrees. By contrast, for a star undergoing accretion, the observed effect would entirely depend on processes within a boundary layer between the stellar surface and the incoming material. The latter possibility, of an interaction between the star and some sort of quasi-disk, seems to be more likely. In addition, the accretion-disk interpretation encounters the main difficulty in the expected size of the disk: For a stable Keplerian disk with the central object of such a small mass as the secondary of AW UMa, the observed separation between the velocity peaks implies disk dimensions of the order of $15\,R_\odot$ (this results from a simple scaling relative to the Earth velocity: $V_d \propto 30\,(M/M_\odot)^{1/2}(215R_\odot/R)^{1/2}$ km s^{-1}). There is no space to accommodate such a large disk. However, we do see – through the *quasi*-Rossiter-McLaughlin effect (Section 4.3) – that gas extends as far from the secondary component in the orbital plane as perhaps to a distance $\simeq 1\,R_\odot$. Thus, most likely, the observed ring-like structure around the secondary component is neither a fully developed Keplerian disk nor a boundary layer on top of the star. It may be an interaction region where the returning matter, which had missed the secondary and already made a full revolution around the primary encounters the one orbiting the secondary component. The losses due to the eventual accretion are replenished by the new matter coming from the relatively nearby L_1 Lagrangian point of the primary component. The amount of the dispersed matter in the orbital plane may be appreciably larger than the rather moderate net mass transfer rate as indicated by the period change.

The complicated accretion flow around the secondary component is visible when velocities are shifted to the expected mass centre for the assumed orbital parameters of the binary. In Figure 14, the 2D images show the secondary component with velocities shifted to its expected mass center for the assumed $K_1 = 28.37$ km s^{-1} and for two values of the mass ratio, $q_{\rm sp} = 0.08$ and 0.10. The motion of the secondary star is very sensitive to $q_{\rm sp}$, so that images such as Figure 14 provide a direct check on the assumed value of $q_{\rm sp}$. The double-peaked structure, which is well defined during the three orbital quadratures (Figure 13), does not seem to continue as a simple,

vertical band in this picture for any of the assumed values of $q_{\rm sp}$, but shows complex changes in brightness and position. The mass ratio $q_{\rm sp} \simeq 0.10$ seems to produce a more stable profile, but there still exist complex motions within the profile which are not in strict anti-phase relation to the primary component. Unfortunately, even the almost-continuous monitoring on three nights did not provide sufficient coverage to establish any regularity in those strands and wobbling motions. Thus estimated mass ratio, $q_{\rm sp} = 0.10$, is basically identical to that determined from the mean positions of the double peak at the orbital quadratures, $q_{\rm sp} = M_2/M_1 = 0.099 \pm 0.003$, where the assumed uncertainty is twice as large as the one formally determined from the mean velocity of the double-peaked structure.

The secondary appears to look much more stable when all the data from the three nights are binned in phase and velocity, as is shown in Figure 15. The individual strands within the accretion structure average out in such an image. The secondary appears to have a somewhat trapezoidal shape bordered by two ridges; the structure follows the expected sine-curve motion of the secondary component for $q_{\rm sp} \simeq 0.10$. In this average, binned image of the whole AW UMa system, the parts which undergo most variability are located in the region of the two peaks in the profile of the secondary component (Figure 16); most of the binary is stable and repeatable. We note that the primary component, except for its surface ripples and spots, is practically invariable anywhere in its velocity field. The pedestal feature is also surprisingly constant with respect to time.

6.2. Dimensions of the secondary

Eclipses have a potential of shedding light on the physical state of AW UMa secondary component. However, in attempting an interpretation, one must remember that the RV data do not tell us anything about geometry of the component stars, but only about the velocities involved. Thus, the shapes in the 2D images require assumptions on how velocities relate to spatial positions. For the secondary component, any interpretation carries an important uncertainty related to the "inside-out" visibility of accretion processes where the largest velocities are expected closest to the star, rather than furthest from it, as expected for rapidly rotating stars.

During the secondary star occultations (the secondary or shallower eclipses) when it disappears behind the large star, the velocity field of the secondary component is hardly modified at all. In Figures 8 – 10, which show deviations from the rotational profile, we can detect slight indentations at the high-velocity edges of the secondary profiles (around phases 0.55, 3.05, 5.05, 5.45, 5.55) which suggest that the highest velocities are cut off. Otherwise, the whole system of radial velocities associated with the secondary component is eclipsed as if it was a single, extended object. The phases of the eclipse contacts are given in Table 5; they were determined by eye from figures similar to Figures 8 – 10. While these determinations carry substantial uncertainty ($\pm$0.01 in phase) due to the presence of the pedestal, the phases of external contact (Contacts 1 and 4 in Table 5) are definitely too large to be identified with the real geometrical contact phases, but – rather – they reflect the large range of velocities in the accretion structure.

The secondary star transits over the disk of the primary component (the primary or deeper eclipses) appear to show contacts which are more similar to what is observed in the photometric light curves. In Figures 8 – 10, the secondary component is visible as two or sometimes three bright ridges which continue the motion of the secondary as observed before and after the eclipses. It is dark inside, but this mainly reflects the imperfect fits of the rotational profile during the transit phases. Although the fits are indeed corrupted, the secondary does produce a very weak disturbance in the primary profiles as can be seen in the last panel of Figure 1. Unfortunately, only one transit was observed exactly during the central eclipses phases (night 3, phase 5.0); however, the two other transits provided moderately well-defined phases of the external and internal contacts (Table 5).

The observations obtained in the center of occultation at phase 5.0 (see Figures 1 and 10), give the velocity extent of the secondary as ranging between -52 and $+52$ km s^{-1}, but with a faint extension reaching on the positive side to $+90$ km s^{-1}. Thus, the full radial-velocity extent of 104 km s^{-1} is larger than the *mean* peak separation during the orbital quadratures, 81 km s^{-1} (Section 6.1), although on one occasion the separation reached 98 km s^{-1}. The amount of the light loss due to the secondary, within the above velocity range is hard to estimate because the depression is very shallow and comparable to depths of the inhomogeneities on the surface of the primary component; very roughly it absorbed 0.05 ± 0.02 of the primary light. This crude estimate, when transformed to linear dimensions gives the linear size of about 0.22 ± 0.05 relative to the size of the primary component. Note, that for the Roche lobes with $q = 0.1$, the ratio of the "side" or orbital-plane dimensions is about 0.35 – 0.36 (weakly depending on the degree of fill-out).

The inner contact phases during the transits when the secondary touches the edges of the primary from inside (Contacts 2 and 3) are distinctly asymmetric relative to the eclipse centre, with the mean values of the phases -0.061 and $+0.034$, see Table 5. While the former is the same as the well determined angle of the photometric internal contact 0.062 ± 0.005 (Mochnacki & Doughty 1972), the exit contact phases are much smaller. The same asymmetry is visible in the "light-curve" of AW UMa in Figure 2. Possibly, it may be explained by the shift in the direction of the mass flow close to the L_1 point which is quite prominent in the model of Oka et al. (2002).

7. AW UMa as a binary system

7.1. Spectroscopic orbital elements

With the orbital velocity amplitude of the primary component $K_1 = 28.37 \pm 0.37$ km s^{-1} (Section 4.3) and the sum of the orbital amplitudes determined from the orbital quadratures, $K_1 + K_2 = 314.2 \pm 3.2$ km s^{-1} (Section 6.1), we find the mass ratio $q_{\rm sp} = M_2/M_1 = 0.0991 \pm 0.0014$, confirming the determination of Pribulla & Rucinski (2008). While this is the best value for the spectroscopic mass ratio, as described previously (Section 6.1), we adopt a two times larger error so that $q_{\rm sp} = M_2/M_1 = 0.099 \pm 0.003$. Even with this adjustment, our spectroscopic mass ratio is several formal errors away from the photometric determinations which usually converge to a

value within $q_{\rm ph} \simeq 0.07 - 0.08$, but with individual errors usually determined very small, as small as 0.0005 (e.g. Wilson (2008)). Using the measured K_1 and following our assumption on $q_{\rm sp}$, the estimated orbital amplitude for the secondary is $K_2 = 286.6 \pm 12.4$ km s^{-1}, the distance between the mass centers $A \sin i = 2.73 \pm 0.11\, R_\odot$, and the masses $M_1 \sin^3 i = 1.292 \pm 0.15\, M_\odot$ and $M_2 \sin^3 i = 0.128 \pm 0.016\, M_\odot$.

The orbital inclination of AW UMa must be close to the edge-on orientation; otherwise we would not see the long-lasting, total eclipses. We certainly cannot assume the orbital inclination angle of $i \simeq 78 - 80$ deg, as determined from light-curve synthesis solutions published over several decades investigation (starting with 80 deg, Mochnacki & Doughty (1972), with the most recent 78 deg, Wilson (2008)), as they all assumed the Lucy contact model. Thus, the above orbit-size and mass determinations may be close to the actual values, but there will remain an additional systematic uncertainty at a level of 1.5% for the linear dimensions and 5% for the masses.

7.2. The evolutionary state

AW UMa appears to be a semi-detached binary showing mass transfer from the more massive to the less massive component. It is not a contact binary as envisaged in the contact binary model of Lucy: The complex internal velocities and obvious accretion processes on or around the low-mass secondary component invalidate the contact model for this binary.

In terms of the evolutionary status of the binary, the new data fully support the models developed by Stępień (2006) and Paczyński et al. (2007). The secondary is probably the helium core of a former more massive component which already evolved past the mass exchange; now it is the formerly less-massive component which expands and sends matter to the small star. In terms of its kinematics and metallicity, AW UMa appears to belong to the local solar population (Rucinski et al. 2013a): the spatial velocity components $[U, V, W] = [12.5 \pm 0.5, -55.5 \pm 4.1, -9.5 \pm 0.5]$ km s^{-1} and the metallicity $[M/H] = -0.01 \pm 0.08$ are typical for an age of 3 – 5 few Gyrs. This age would be long enough to produce a system already in the stage of the former secondary expanding beyond its Roche limit.

With its systematically shortening orbital period, AW UMa appears to be evolving towards an eventual merger. Thus, in the time scale of $(d \ln P/dt)^{-1} \simeq 2 \times 10^6$ years, AW UMa will show an eruption and coalescence in the same way as was observed and analyzed recently by V1309 Sco (Tylenda et al. 2011; Stępień 2011; Pejcha 2014).

8. Conclusions and directions for further research

Except for the important conclusion that AW UMa is not a contact binary, but a semi-detached system, the present work has produced more questions than answers... First of all, the above

conclusion leads to a major disagreement with the excellent explanation of its light curve by the Lucy contact-binary model. Why do the light curve synthesis models, based on the contact model, give such perfect reproductions of the AW UMa light curves and yet spectroscopy gives an entirely different, complex picture with many asymmetries and variations within a semi-detached binary? Is something missing in the current analysis?

The phase dependence of the integrated Broadening Functions indicates that most of the photometric variations are produced by the same material; one can even restore the light curve assuming the constancy of the primary component (the remaining difference is 3% for the full 19% photometric modulation). Thus, we seem to see the same matter which causes light variations and produces spectra. Of course, it is true that symmetric mass distribution (along the line of mass-centers) may still contain (and hide) asymmetric motions and that the BF method is only sensitive to velocities. But are the discrepancies not too large? This major disagreement requires further study because rejection of the contact model should not be done too hastily: It is a conceptually simple and consistent model which apparently has worked well since its inception in 1968 (Lucy 1968a,b). But the model still requires rigorous tests on its applicability; the observations such as those presented here for other W UMa-type binaries would be most useful. After all, the current study is the first in-depth, high-resolution, high signal-to-noise, spectroscopic study of a W UMa binary. Because of the rapid variations, high-resolution spectroscopic studies require allocation of time on large telescopes, at least of the 4-meter class, together with efficient spectrographs. The most obvious target for such a study would be ϵ CrA, the brightest W UMa binary in the sky ($V = 4.8$). Its period is slightly longer (0.591 d) and the spectral type later (F3), but it can be considered almost a twin of AW UMa in that it also shows total eclipses and its mass ratio is small. The spectroscopic study of Goecking & Derbeck (1993) led to determination of masses, both slightly larger than that of AW UMa, but it was conducted at too low a resolution, $R \simeq 10,000$, to be able to reveal complexities as extensive as those observed for AW UMa. It is interesting that the spectroscopic mass ratio was also found for ϵ CrA to be larger than the photometric one.

While the primary component of AW UMa seems to be a simple, fast rotating, non-variable F2V star, it shows unexpected features when analyzed in greater detail: The current work has confirmed the existence of the "pedestal" of large rotational/orbital velocities around the primary and of numerous inhomogeneities on its surface. Stępień (2009) has already given an explanation of the pedestal in terms of the extensive equatorial-plane flow which results from the mass-exchange process in the binary; the study was partly inspired by the previous analysis of AW UMa by Pribulla & Rucinski (2008). The pedestal, which reaches a total intensity of about 4% of the primary star, is surprisingly constant between the individual orbital cycles. In addition, it shows the double-cosine variability which is in phase with the photometric ellipticity effect. The pedestal seems to be the only phase-dependent feature which shows a full symmetry along the axis joining the stars. The inhomogeneities on the primary were suspected in the data of Pribulla & Rucinski (2008), but only now, with continuous temporal coverage on three consecutive night have they been seen in full detail. The dense network of the "ripples" has no immediate explanation. The ripples

share the photospheric rotation of the primary yet they seem to extend into the pedestal; their amplitudes grow toward lower spatial frequencies. The "spots" are equally mysterious: Why do they appear only at negative velocities? What are they? Unfortunately, our analysis leaves room for interpretation as the dark notches in the BF's may equally be caused by genuine photospheric dark spots as well as locally shallower spectral lines, either due to higher temperatures or to filling-in by emissions. The very slow rotation of the spots suggests their participation in a strongly differential rotation, perhaps by $\simeq 50\%$ slower than the star itself; why then don't we see any discrepancies in the rotational-profile fits which imply a consistent value of $V \sin i = 181$ km s^{-1}?

The secondary component shows complex accretion phenomena. It appears as a system of bands or strands which change in time so it is hard to tell what the actual shape of the star is. It must be very small, as its transits in front of the primary produce very small line-profile effects. The local centre of velocities, which we identify as the secondary component, moves as for the binary mass ratio $q_{\rm sp} = M_2/M_1 = 0.099 \pm 0.003$. This is a result many formal errors away from the previous, photometric, very consistent determinations. Which value is the correct one? Is this because the light curves have a relatively low information content and we only now have a proper dynamical determination? The light curves are indeed featureless except for the well defined inner eclipse contact, whose phase very strongly constraints the synthesis solutions, particularly the value of $q_{\rm ph}$. While we do see inner eclipse contacts also in velocities, they appear to be different than the photometric ones and variable from eclipse to eclipse. The mean velocities of the secondary component permit determination of minimum masses for the components of AW UMa: $M_1 \geq 1.29 \pm 0.15\, M_\odot$ and $M_2 \geq 0.128 \pm 0.016\, M_\odot$ which are most likely very close to the actual ones because the orbit is seen close to the edge-on orientation.

As was said above, this study has led to more questions than answers. While the evolutionary and physical state of AW UMa is moderately simple, the many new features discovered in the detailed view of AW UMa require further investigation. Further studies based on the same excellent CFHT spectra are planned as the followup of the current work.

The author would like to express his most sincere thanks to several individuals who helped him during this work either directly or through extensive discussions and comments: Jano Budaj, Jean-Francois Donati, Nadine Manset, Theo Pribulla, Michał Różyczka, Kazik Stępień, Bob Wilson, Walter Van Hamme, Gemma Whittaker.

Thanks are due to the reviewer of the first version of the manuscript for the very pointed and constructive comments and suggestions.

The research of the author has been supported by the Natural Sciences and Engineering Research Council of Canada. This research made use of the SIMBAD database, operated at the CDS, Strasbourg, France and of NASA's Astrophysics Data System (ADS).

REFERENCES

Donati, J.-F., & Collier Cameron, A. 1997, MNRAS, 291, 1

Donati, J.-F., Semel, M., Carter, B.D., Rees, D.E., Collier Cameron, A. 1997, MNRAS, 291, 658

Gray, D. F. 2005, The Observation and Analysis of Stellar Photospheres, 3rd Edition (Cambridge: Cambridge University Press)

Goecking, K.-D., & Duerbeck, H. W. 1993, A&A, 278, 463

Hilditch, R. W., 2001, An Introduction to Close Binary Stars, (Cambridge: Cambridge University Press)

Kubiak, M., Udalski, A., Szymański, M. K. 2006, Acta Astr., 56, 253

Lucy, L.B. 1968a, ApJ, 151, 1123

Lucy, L.B. 1968b, ApJ, 153, 877

McLean, B. J. 1981, MNRAS, 195, 931

Mochnacki S.W., & Doughty N.A. 1972, MNRAS, 156, 51

Oka, K., Nagae, T., Matsuda, T., Fujiwara, H., & Boffin, H. M. J. 2002, A&A, 394, 115

Paczyński B. 1964, AJ, 69, 124

Paczyński B., Sienkiewicz, R., & Szczygieł, D. M. 2007, MNRAS, 378, 961

Pejcha, O. 2014, ApJ, 788, 22

Pribulla, T., Chochol, D., Rovithis-Livaniou, H., & Rovithis, P. 1999, A&A, 345, 137

Pribulla, T., & Rucinski, S. M. 2008, MNRAS, 386, 377

Rensing M. J., Mochnacki S. W., & Bolton C. T. 1985, AJ, 90, 767

Rucinski S. M. 1992, AJ, 104, 1968

Rucinski, S. M. 2010, ASP Conf., 435, 195

Rucinski, S. M. 2012, in From Interacting Binaries to Exoplanets: Essential Modeling Tools, IAU Symp. 282, M. Richards and I. Hubeny (eds), p.365

Rucinski S.M., Pribulla, T., & Budaj, J. 2013, AJ, 146, 70

Rucinski S. M. 2013, Inf. Bull. Var. Stars, 6079

Smak, J. 1981, Acta Astr., 31, 395

Smak, J. 1993, Frontier Objects in Astrophysics and Particle Physics, eds. F. Giovanelli & G. Mannocchi, (Soc. Italiana Phys., Bologna), p.81

Stępień, K. 2006, Acta Astr., 56, 199

Stępień, K. 2009, MNRAS, 397, 857

Stępień, K. 2011, A&A, 531, A18

Tylenda, R., Hajduk, M., Kamiński, T., Udalski, A, et al. 2011, A&A, 531, A18

Wilson, R. E., & Devinney, E. J. 1973, ApJ, 182, 539

Wilson, R. E. 2008, ApJ, 672, 575

This preprint was prepared with the AAS LaTeX macros v5.2.

Table 1. Observations of AW UMa

Date 2011	Range	ϕ	N
11 March	55,631.850 – 55,632.146	0.456 – 1.131	152
12 March	55,632.746 – 55,633.147	2.499 – 3.412	200
13 March	55,633.781 – 55,634.141	4.858 – 5.567	232

Note. — The time range for mid-exposures is expressed as $HJD - 2,400,000$; ϕ gives the range in phase computed from the assumed initial epoch $HJD = 2,455,631.6498$ and $P = 0.43872420$ day; N is the number of spectra obtained on a given night.

Table 2. Broadening Functions

	−4950	−4932	−4914	−4896	−4878	−4860	...
18497	−700	−400	−49	128	141	106	...
18512	−959	−716	−362	−87	76	135	...
18527	−821	−643	−348	−110	8	15	...
...							

Note. — This table is available in the on-line version only.
For efficient transfer, the ASCII file has all numbers scaled and converted to integers. The first row gives 551 velocities in the heliocentric system, expressed in km s^{-1} and multiplied by 10 (format: 6x,551i6). The subsequent 584 rows (format: 552i6) give, in the first position, the time $HJD - 2\,455\,630$ multiplied by 10^4, and then 551 values of the Broadening Function multiplied by 10^6. Thus, the velocities in the first row are: −495.0, −493.2, −491.4, −489.6, −487.8, −486.0, ... km s^{-1} and the corresponding BF values at $T = 1.8497$ are: −0.000700, −0.000400, −0.000049, 0.000128, 0.000141, 0.000106.

Table 3. Radial velocities of the primary component

T	ϕ	V_1^{45}	V_1^{50}	V_1^{55}
1.8497	0.4556	−22.40	−22.20	−21.19
1.8512	0.4590	−22.60	−23.30	−23.20
1.8527	0.4624	−22.50	−22.96	−23.06
1.8542	0.4658	−22.69	−23.33	−23.00
1.8559	0.4697	−20.46	−21.02	−21.27
...				

Note. — This table is available in the on-line version only.
The mid-exposure times are given as $T = HJD - 2\,455\,630$, while the phases are computed with the assumed initial epoch $HJD = 2,455,631.6498$ and the period 0.43872420 day. RV measurements for all observations are listed, but only those within the fractional phase interval 0.25 – 0.75 were used for the orbital solutions. The primary star velocities (in km s^{-1}) are given in the three columns labeled V_1^{45}, V_1^{50} and V_1^{55} corresponding to the low cut-off to the rotational profile fit at 0.45, 0.50 and 0.55 of the BF maximum.

Table 4. Orbital solutions for the primary component

Cut-off	V_0	K_1	σ_1
0.45	-15.78 ± 0.06	28.67 ± 0.085	0.99
0.50	-15.90 ± 0.07	28.33 ± 0.102	1.20
0.55	-16.01 ± 0.08	28.12 ± 0.115	1.34
Mean	-15.90 ± 0.12	28.37 ± 0.37	

Note. — The rotational profile fits were done above the Cut-off level expressed relative to the BF maximum. σ_1 is the fit error for one observation. All velocities are in km s^{-1}. The errors for the Mean values represent the rms scatter of the determinations, not the formal Gaussian errors of the mean (i.e. divided by $\sqrt{(3)}$), because the deviations are systematic.

Table 5. Eclipse contact phases

2011	Contact 1	Contact 2	Contact 3	Contact 4
Transit				
11 March	$-0.150 + 1$	$-0.062 + 1$	$+0.032 + 1$	$+0.128 + 1$
12 March	$-0.129 + 3$	$-0.060 + 3$	$+0.034 + 3$	$+0.128 + 3$
13 March	$-0.140 + 5$	$-0.060 + 5$	$+0.037 + 5$	$+0.117 + 5$
Occultation				
11 March	···	···	$+0.044 + 0.5$	$(+0.110) + 0.5$
12 March	$(-0.160) + 3.5$	···	$(+0.055) + 2.5$	$(+0.133) + 2.5$
13 March	$(-0.140) + 5.5$	$-0.064 + 5.5$	$+0.054 + 5.5$	···

Note. — Phases of contacts are given from the first outer Contact 1, through the two inner Contacts 2 and 3 to the outer Contact 4. The format for the phases, with separately expressed integer parts, is used to emphasize the phase difference relative to the eclipse center yet retain information on when the eclipse was observed within the run. Errors in phase are about 0.005 for transits and about 0.01 for occultations; values less accurate are in parentheses.

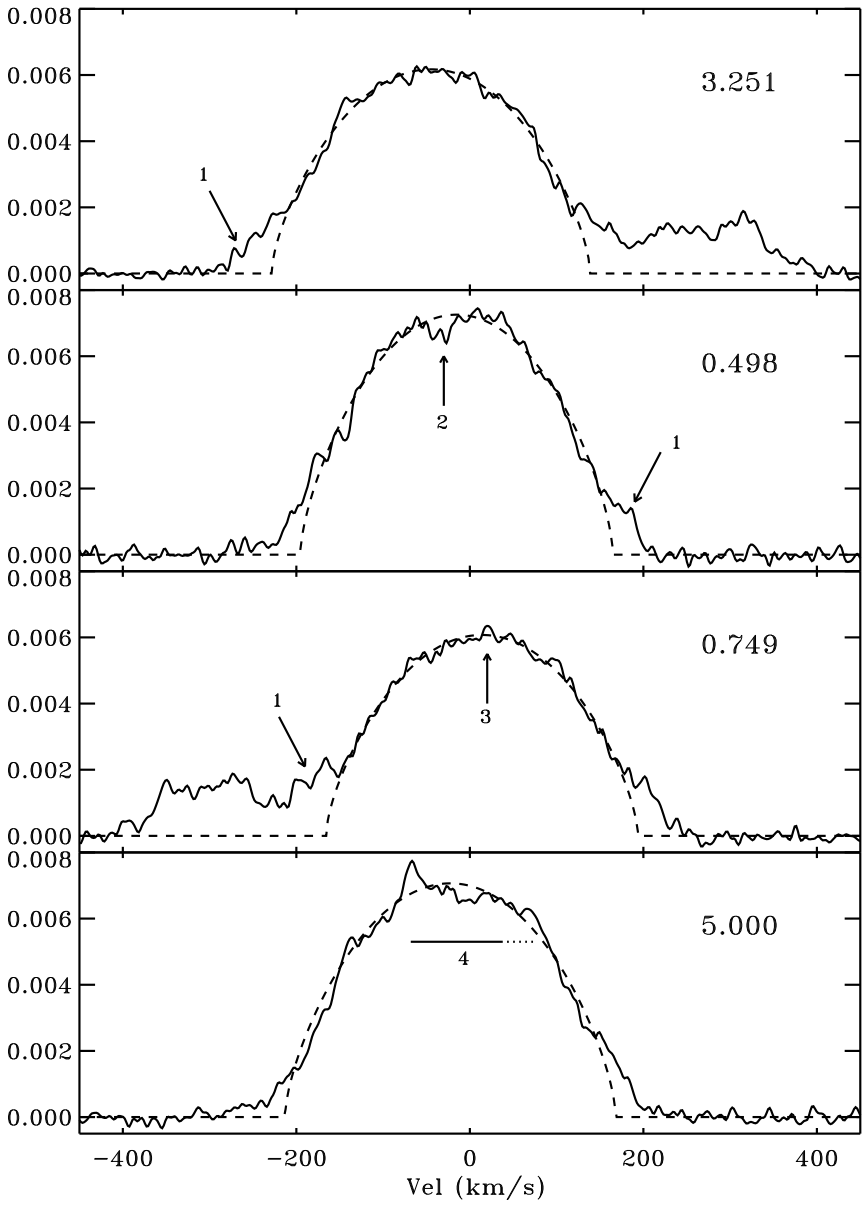

Fig. 1.— Broadening Functions for four individual observations closest to the orbital quadratures and the eclipse centers. The phases – counted from the primary eclipse before the start of the observations – are given in the figure panels. Velocities in the horizontal axis are in the heliocentric system. Units of the BF's in the vertical scale result from their normalization of the integral to unity for the exact spectral match of the template when sampled at 1.8 km s^{-1} (see the text). For AW UMa, the integral is almost constant in phase and close to 1.1 (see the lower panel of Figure 2). The surface features on the primary component which are discussed in detail in the paper are indicated by the numbers: 1 – the pedestal, 2 – a typical spot, 3 – surface ripples, 4 – the secondary component projecting onto the primary star (see Section 6). The broken lines give the rotational profiles which were fit to the upper 45%, 50% and 55% of the primary feature to obtain radial velocities of the primary component.

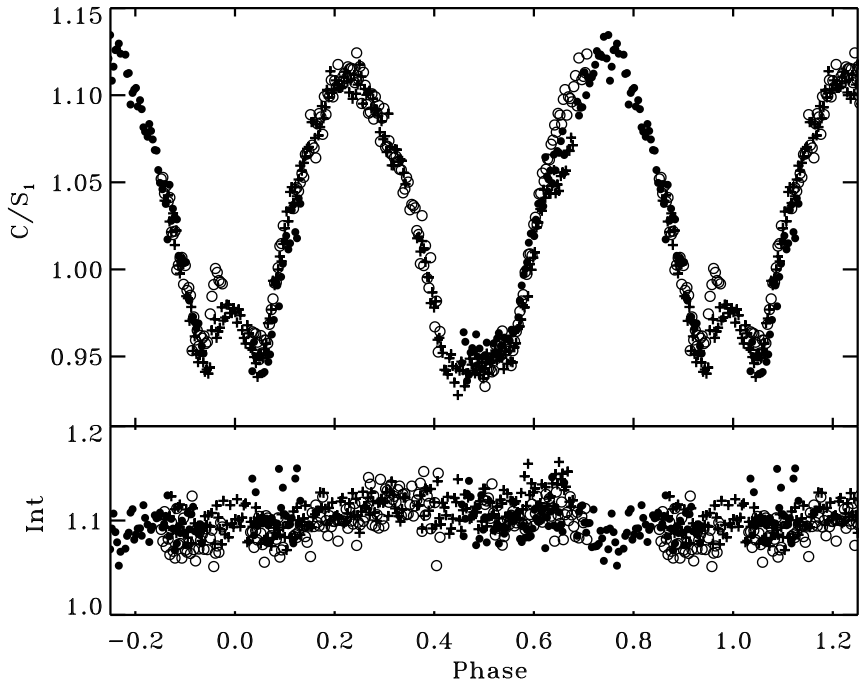

Fig. 2.— The upper curve shows the values (shown as inverses) of the central strength of the fitting rotational profile for the primary component, S_1; they are normalized to the integral of the rotational profile (the constant C, see the text). The symbols correspond to the three nights: night #1, filled circles; night #2, open circles; night #3, crosses. The lower curve shows the integrals of the BF's.

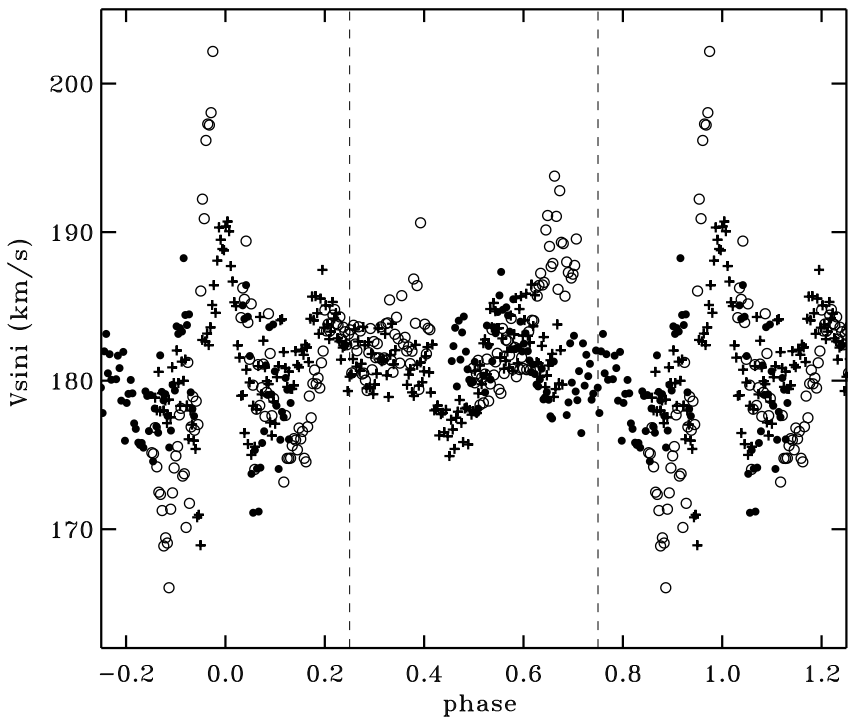

Fig. 3.— The $V \sin i$ values determined by rotational-profile fits to the upper 50% of the primary component BF feature. The symbols for the three nights are the same as in Figures 2. The median value of $V \sin i$ was determined within the phase range $0.25 < \phi < 0.75$.

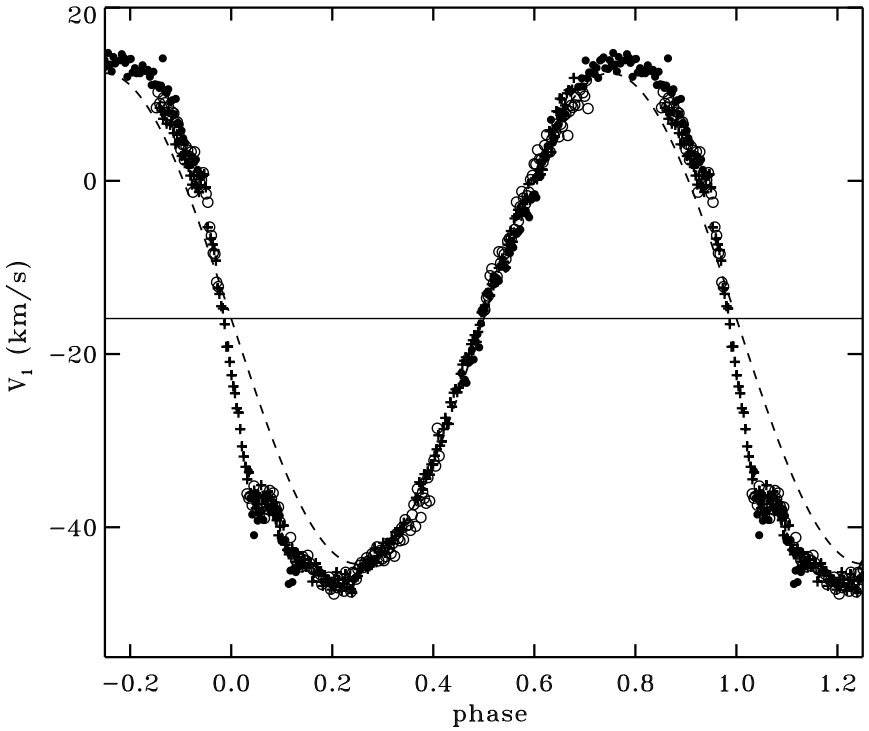

Fig. 4.— Radial velocities of the primary component of AW UMa determined by rotational-profile fits to the upper 50% of the primary feature. The symbols for individual nights are the same as in Fig. 2 and 3. The broken line gives the sine-curve fitted in the phase range $0.25 < \phi < 0.75$ with the parameters averaged from three sets based on the profile fits done at three different cutoffs of the fitting rotational profile, as discussed in the text.

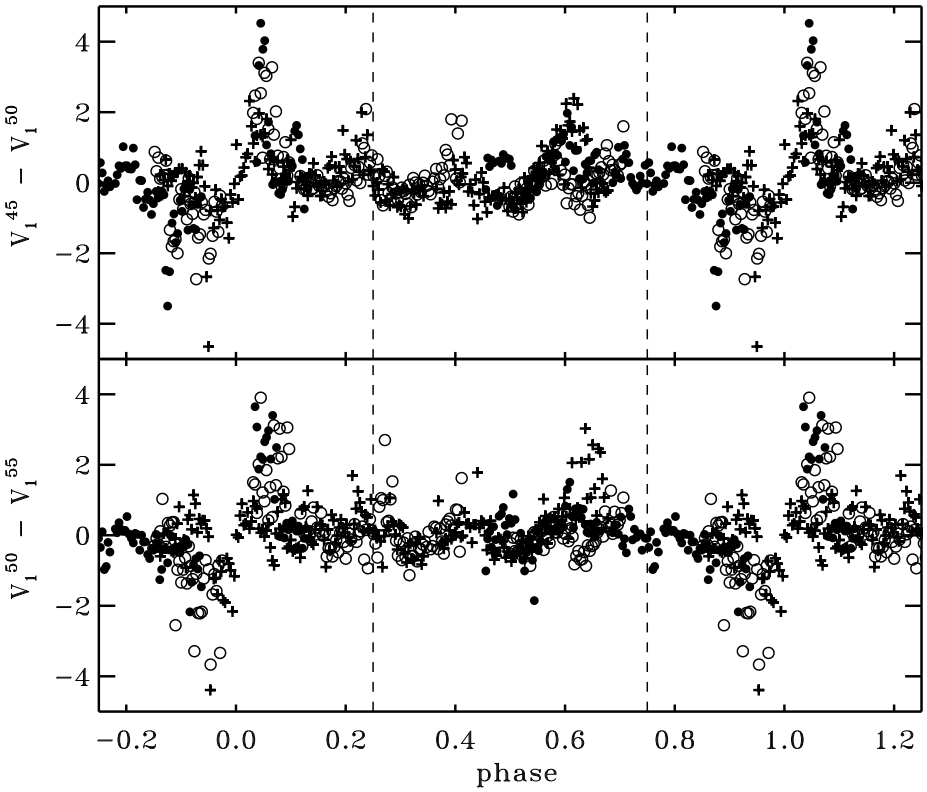

Fig. 5.— Differences of the radial-velocity measurements of the AW UMa primary component, $V_1^{45} - V_1^{50}$ and $V_1^{50} - V_1^{55}$, as measured by rotational-profile fits with a cut-off levels set at 0.45, 0.50 and 0.55 of the BF maximum. The symbols for the individual nights are the same as in the previous figures. The vertical broken lines delineate the phase range $0.25 < \phi < 0.75$ used for three independent sine-curve fits.

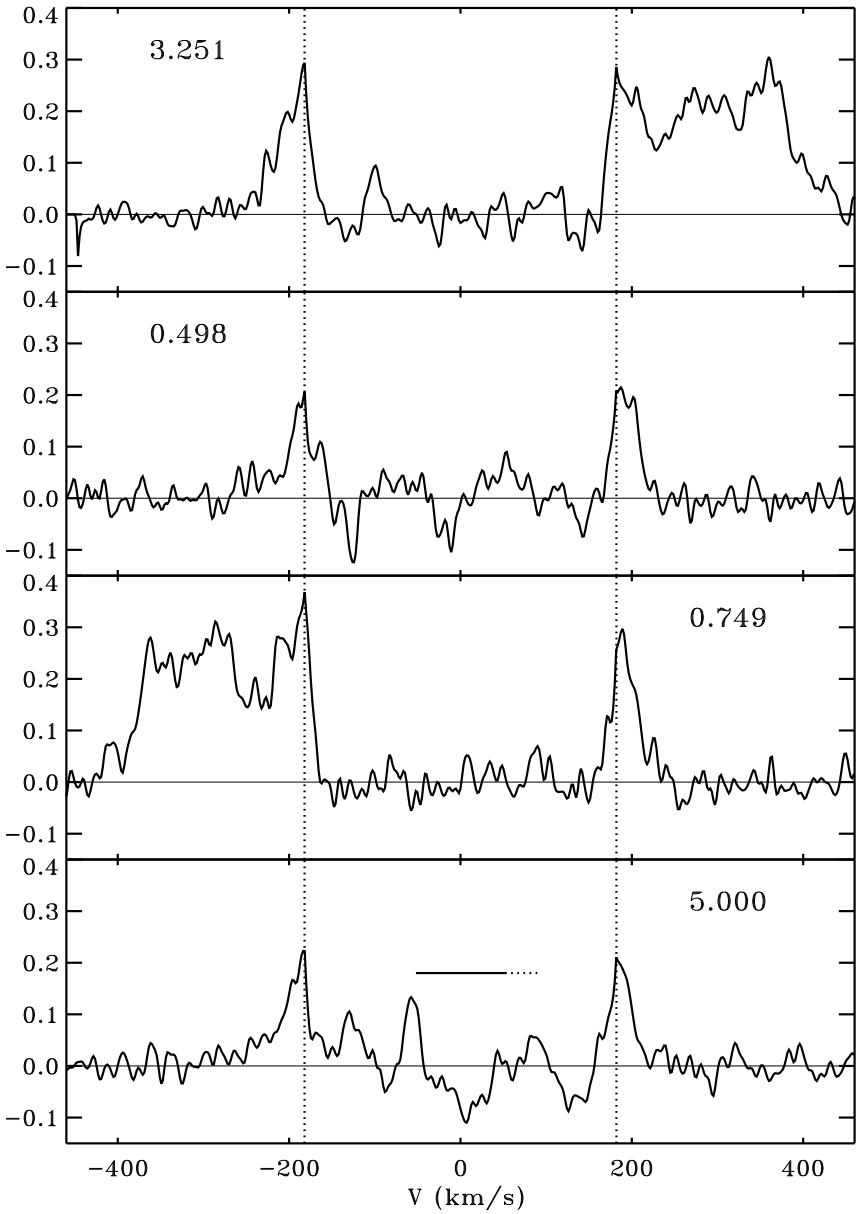

Fig. 6.— Deviations from the fits of the rotational profile to the primary component are shown here for the same phases as in Figure 1. The "pedestal" is the additional light at and beyond the limit defined by $V \sin i = 181.4$ km s^{-1} (marked by the vertical dotted lines). The velocity system is shifted to the centre of the primary component. In this and in the subsequent figures the vertical axis is in intensity units (i.u.) of the central brightness of the primary component. The range, where the secondary component appears to be projected onto the primary star (see Section 6), is shown by a horizontal bar in the last panel.

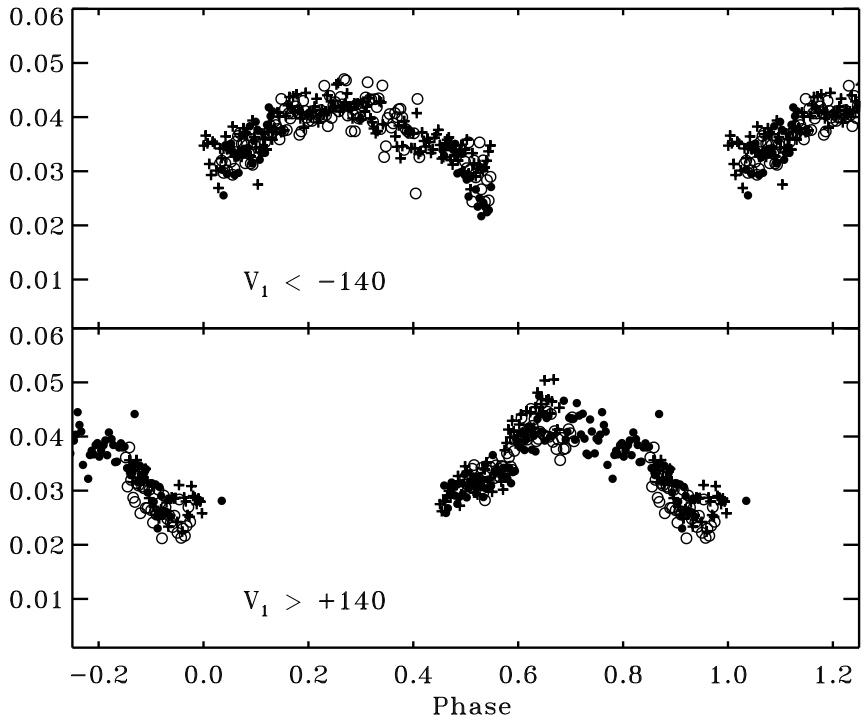

Fig. 7.— The flux of the pedestal integrated between velocities $-250 < V_1 < -140$ km s^{-1} (the upper panel) and $+140 < V_1 < +250$ km s^{-1} (the lower panel), expressed relative to the integrated flux within the rotational profile of the primary component. The symbols used for the three nights are the same as in the previous figures.

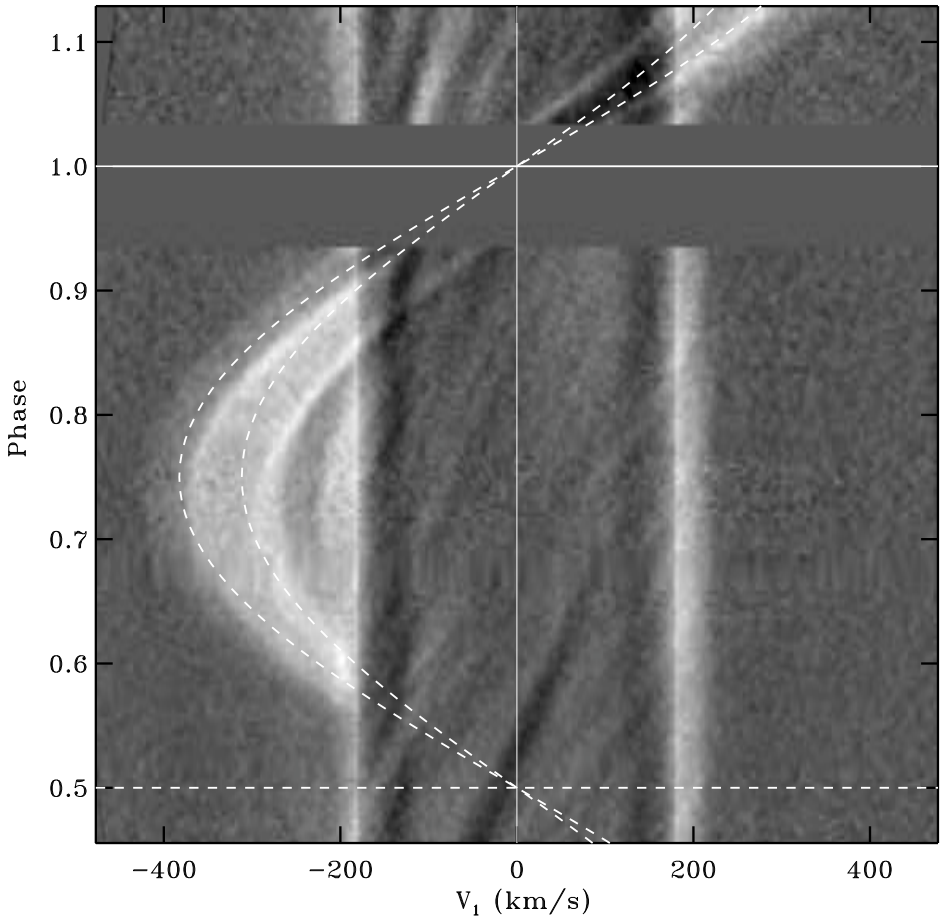

Fig. 8.— The two-dimensional representation of variations in the Broadening Functions of AW UMa versus the orbital phase for the first night of the CFHT run. The horizontal axis is the velocity relative to the center of the primary component while the vertical axis is the orbital phase counted uniformly through the observing run. The BF's for the primary component have the same (scaled in amplitude) rotational profile $V \sin i = 181.4$ km s^{-1} subtracted to improve the visibility of the surface inhomogeneities. The dark, strongly inclined feature at the bottom of the figure ($\phi \simeq 0.5$, $V_1 \simeq 0$ km s^{-1}) is a spot. The ripples form a tenuous grid of slightly less steeply inclined, weaker lines. The continuous broken lines represent the expected motion of the secondary component for two mass ratios, $q = 0.10$ and 0.08; the amplitude is larger for the smaller q. The grey area close to phase 1.0 in the upper part of the figure corresponds to phases which were not observed.

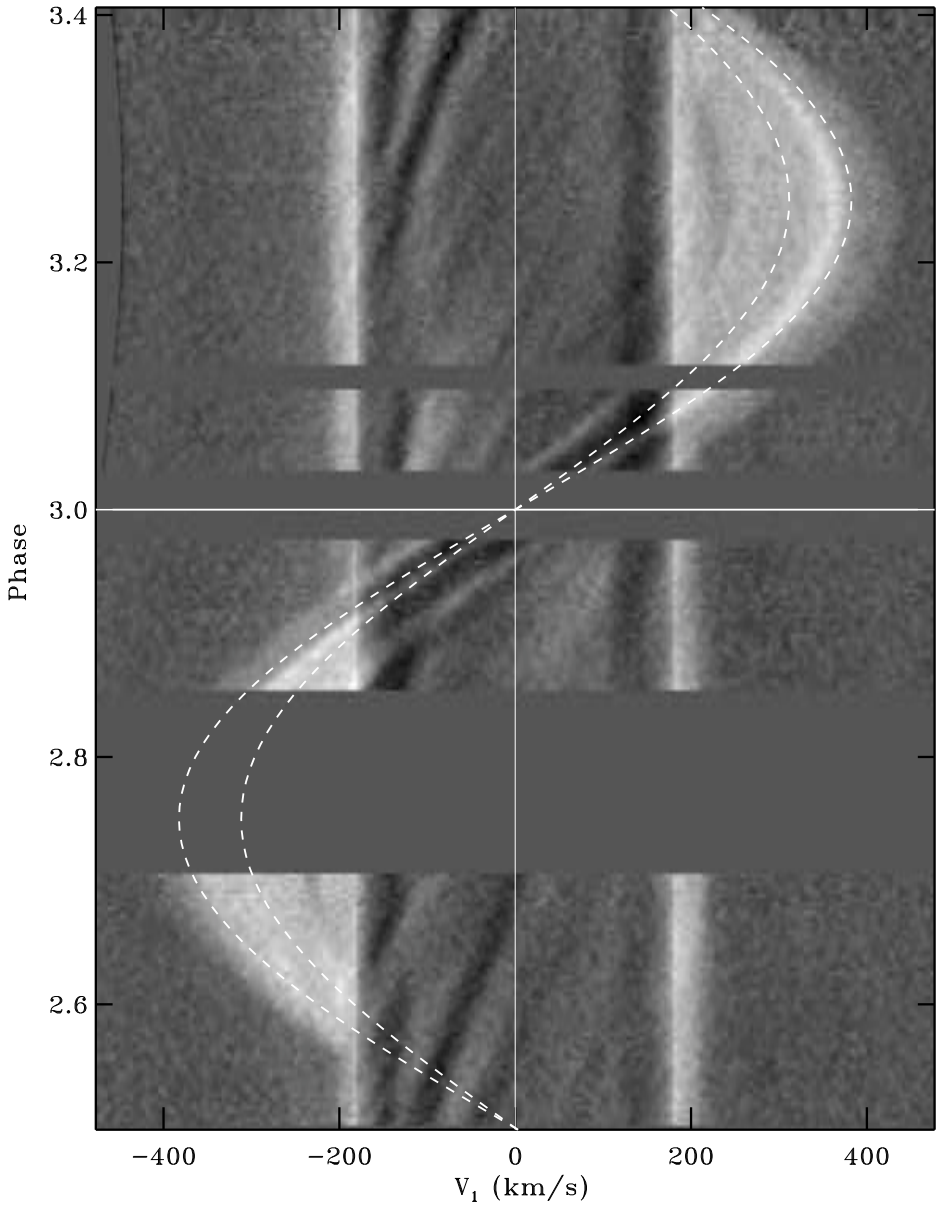

Fig. 9.— The same as for Figure 8 for the second night of the CFHT run.

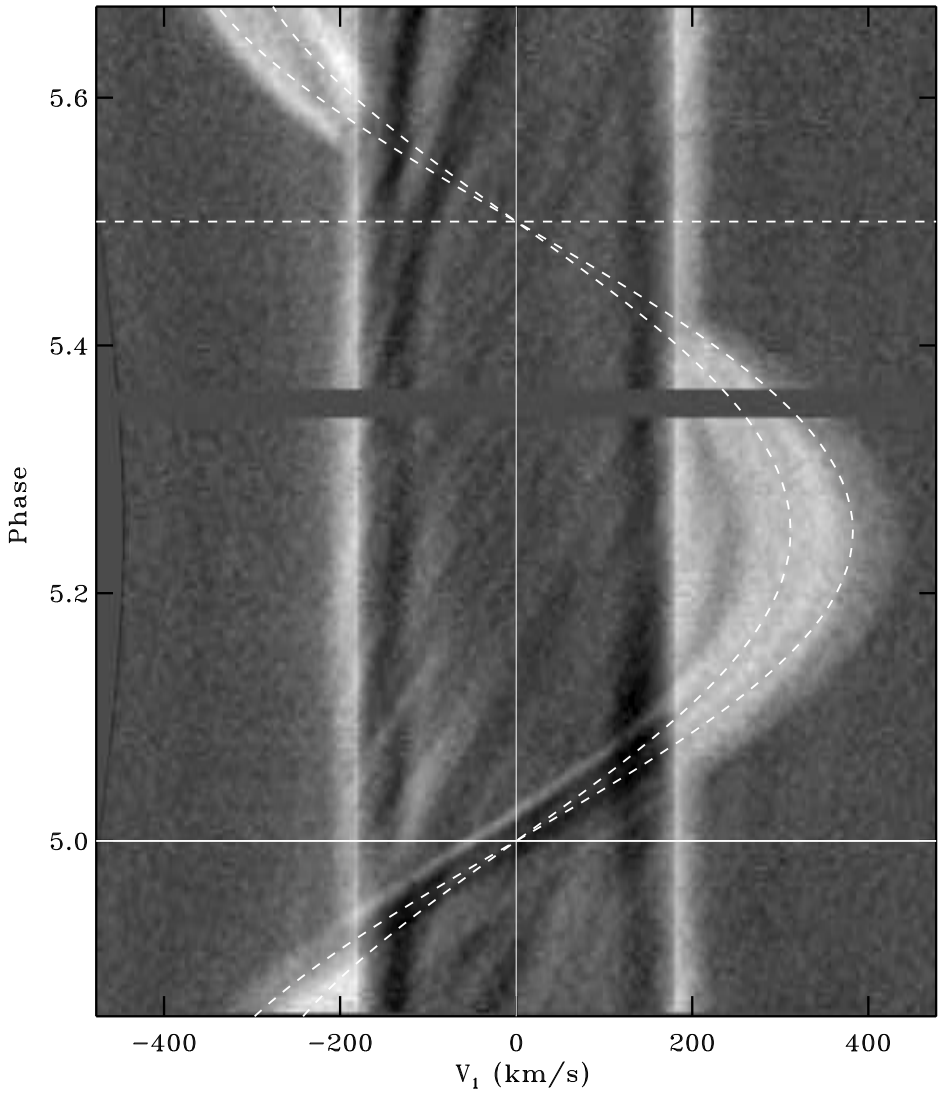

Fig. 10.— The same as for Figure 8 for the third night of the CFHT run.

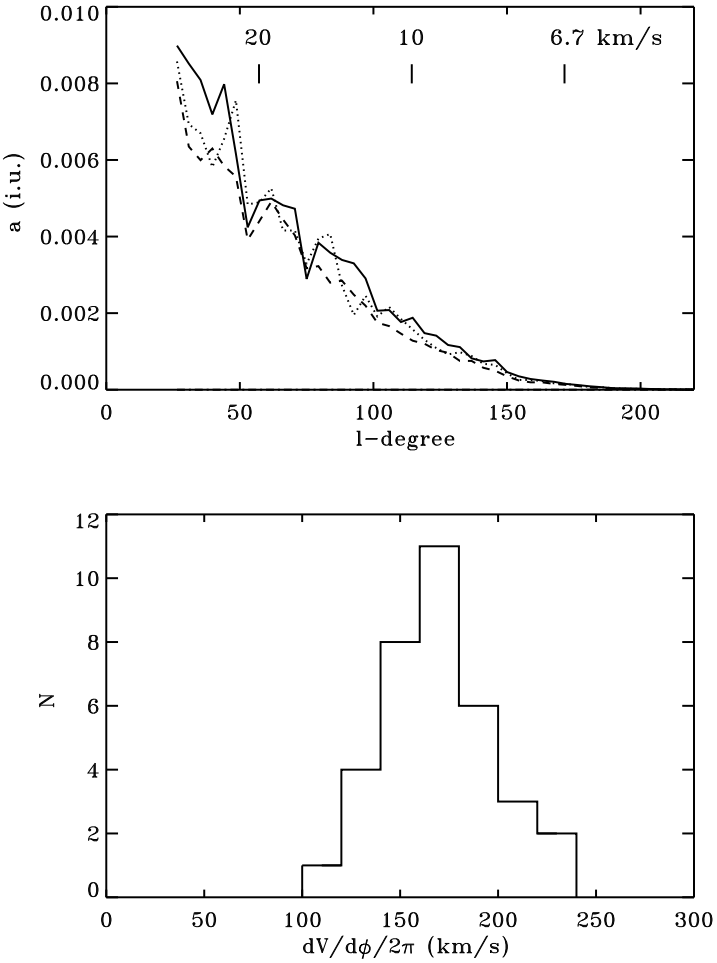

Fig. 11.— The upper panel shows the amplitudes of spatial frequencies (in radial velocity space) for the surface ripples within four phase sections, as described in the text. The horizontal axis is in the angular degrees, l, as typically used for description of non-radial pulsations. The intensity unit (i.u.) for the amplitudes is the brightness of the primary star at the centre of its BF profile. The size of the corresponding features in radial velocities is given along the upper horizontal axis. Note that the resolution of the BF's was set at 8.5 km s^{-1} so that fluctuations with $l > 135$ represent noise. The lower panel gives the histogram of the drift velocities at the central meridian for the best defined ripples, typically seen at the contrast of at least 0.005 – 0.007 i.u.

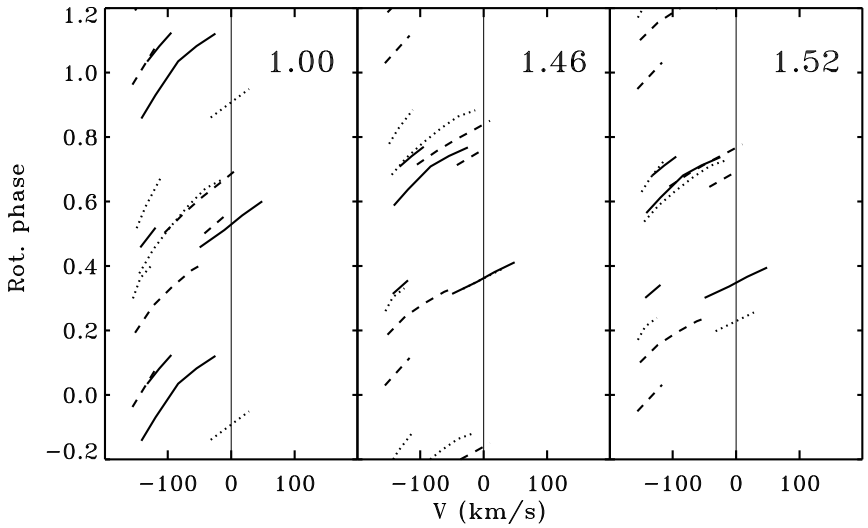

Fig. 12.— The spot drift diagrams in the velocity vs. the rotational phase for the assumed three rotation periods of the spots: $P_{\rm orb}$, $1.46 \times P_{\rm orb}$ and $1.52 \times P_{\rm orb}$. The lines give the spot positions for the three nights: continuous – night #1; dashed – night #2; dotted – night #3. The spots usually disappeared before the meridian transit seldom reaching positive velocities.

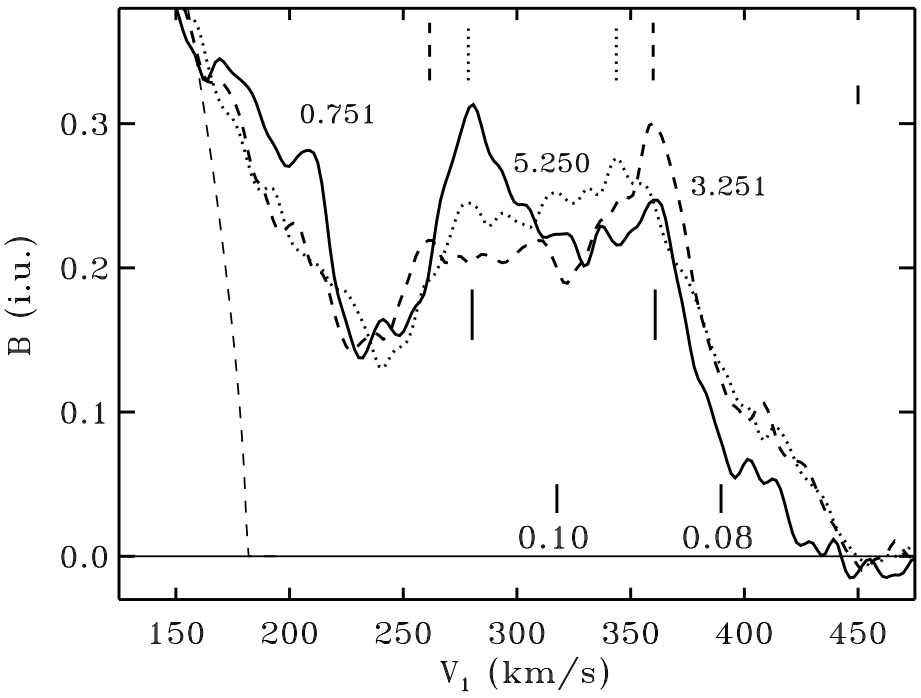

Fig. 13.— The secondary component, as visible in radial velocities within ±0.015 of the three observed orbital quadratures. The velocities are relative to the primary component; the steep, broken, thin line at the left of the figure gives the rotational profile of the primary. Of the three quadratures, two were observed with the secondary receding from the observer (the nights #2 and #3, phases 3.251 and 5.250) and one quadrature was observed with the secondary approaching the observer (the night #1, phase 0.751; for this night the velocity scale was inverted). The different lines are used: continuous – night #1; dashed – night #2; dotted – night #3. The pairs of corresponding vertical bars mark positions of the accretion profile peaks on those nights. The error bars resulting form averaging of 9 individual BF's for each case are not shown for clarity of the figure; the median value of the error, 0.0065 i.u., is shown as a short vertical bar in the upper right corner. The markers 0.08 and 0.10 in the lower part of the figure give the predicted positions of the secondary centroid (i.e. $K_1 + K_2$) for the measured amplitude K_1 and the two values of the mass ratio q.

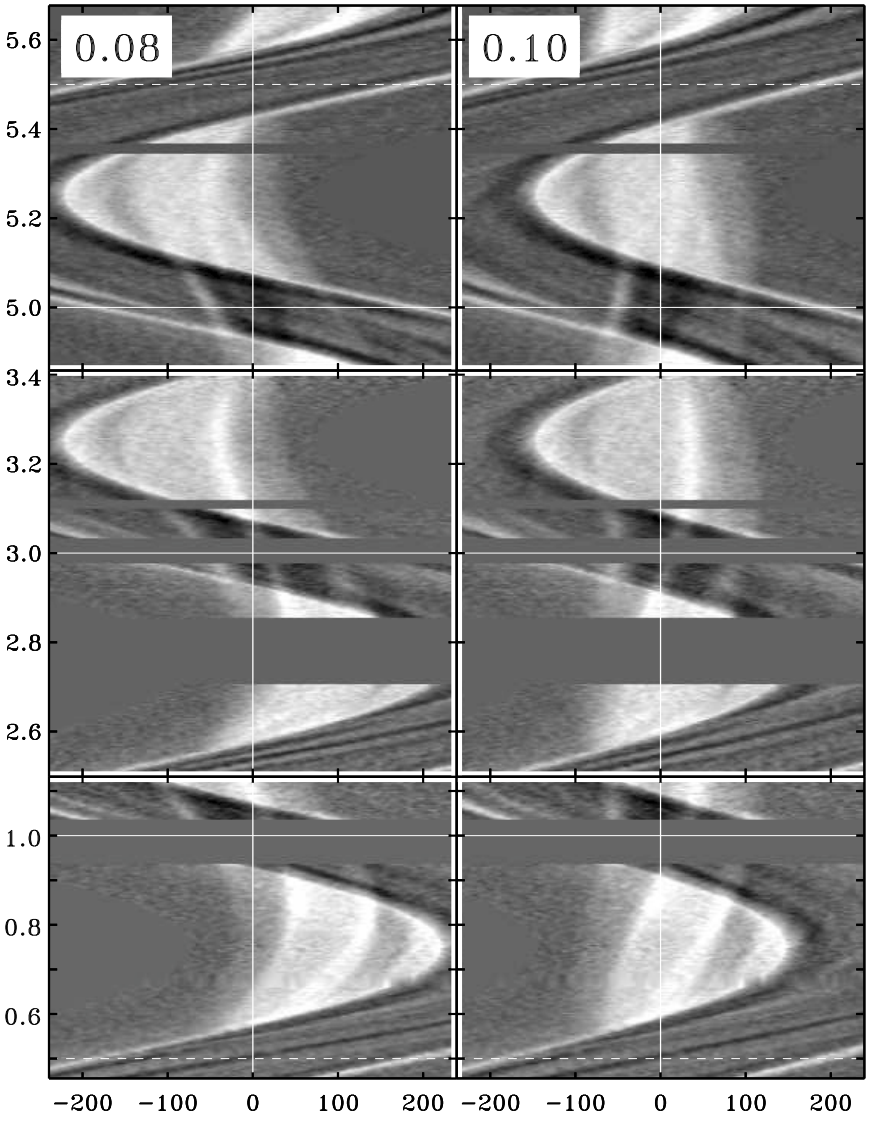

Fig. 14.— The two-dimensional images of the secondary component of AW UMa in velocity space, similar to Figures 8 – 10, but with the velocity system shifted to the expected motion of the secondary component centroid for two values of the mass ratio, 0.08 and 0.10, as marked for vertically arranged panels. The horizontal solid and broken white lines mark the phases of the primary and secondary eclipses.

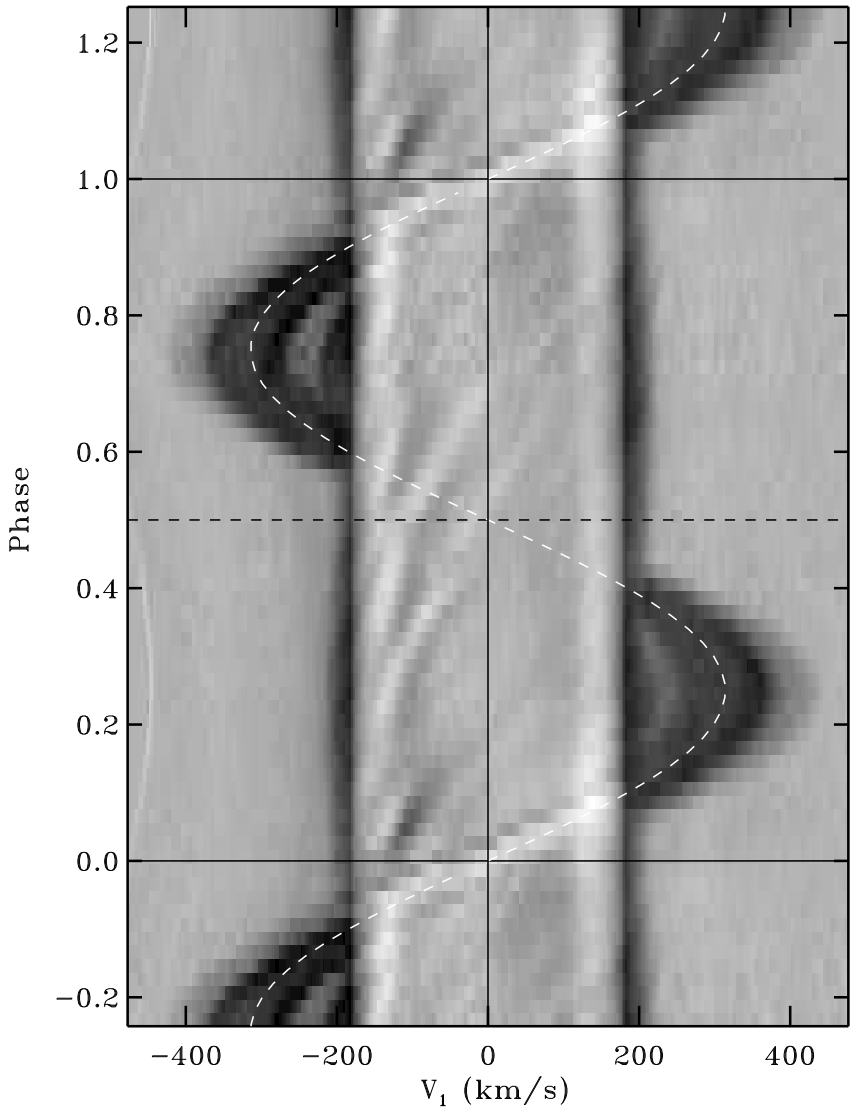

Fig. 15.— The two-dimensional image of the AW UMa system for all data binned and averaged in phase and velocity. The horizontal axis gives velocities in the system centered on the primary component. The sine curve gives the expected motion of the secondary for $K_1 + K_2 = 315$ km s^{-1} (or $q = 0.099$).

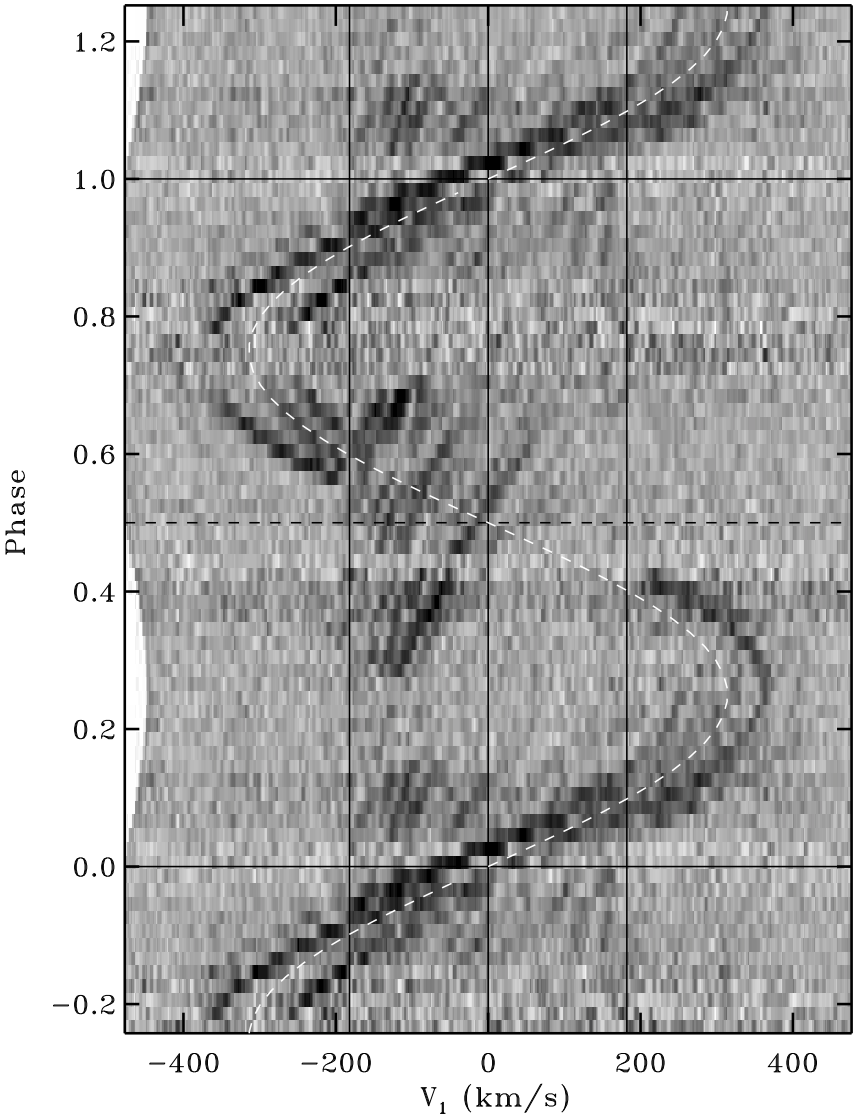

Fig. 16.— The figure gives the standard deviations in the binned data as shown in Figure 15. Note that the most variable regions are the peaks in the accretion structure around the secondary component and the spots on the primary component (best visible for phases $0.35 < \phi < 0.65$). It is significant that the primary and – in particular – the pedestal around it do not seem to be variable in the night-to-night timescale.